

Atomic motifs govern the decoration of grain boundaries by interstitial solutes

Xuyang Zhou^{1,2,*}, Ali Ahmadian², Baptiste Gault^{1,3}, Colin Ophus⁴, Christian H. Liebscher², Gerhard Dehm², Dierk Raabe^{1,*}

[1] Department of Microstructure Physics & Alloy Design, Max-Planck-Institut für Eisenforschung GmbH, 40237 Düsseldorf, Germany.

[2] Department of Structure & Nano- / Micromechanics of Materials Max-Planck-Institut für Eisenforschung GmbH, 40237 Düsseldorf, Germany.

[3] Department of Materials, Royal School of Mines, Imperial College London, SW7 2AZ London, UK.

[4] National Center for Electron Microscopy, Molecular Foundry, Lawrence Berkeley National Laboratory, Berkeley, California 94720, USA

*Corresponding to: x.zhou@mpie.de; d.raabe@mpie.de;

Abstract

Grain boundaries, the two-dimensional (2D) defects between differently oriented crystals, control mechanical and transport properties of materials¹⁻³. Our fundamental understanding of grain boundaries is still incomplete even after nearly a century and a half of research since Sorby first imaged grains⁴. Here, we present a systematic study, over 9 orders of magnitude of size scales, in which we analyze 2D defects between two neighboring crystals across five hierarchy levels and investigate their crystallographic, compositional, and electronic features. The levels are (a) the macroscale interface alignment and grain misorientation (held constant here); (b) the systematic mesoscopic change in the inclination of the grain boundary plane for the same orientation difference; (c) the facets, atomic motifs (structural units⁵), and internal nanoscopic defects within the boundary plane; (d) the grain boundary chemistry; and (e) the electronic structure of the atomic motifs. As a model material, we use Fe alloyed with B and C⁶, exploiting the strong interdependence of interface structure and chemistry in this system. This model system is the basis of the 1.9 billion tons of steel produced annually⁷, and has an eminent role as a catalyst⁸. Surprisingly, we find that even a change in the inclination of the GB plane with identical misorientation impacts GB composition and atomic arrangement. Thus, it is the smallest structural hierarchical level, the atomic motifs, which control the most important chemical properties of the grain boundaries. This finding not only closes

a missing link between the structure and chemical composition of such defects but also enables the targeted design and passivation of the chemical state of grain boundaries to free them from their role as entry gates for corrosion ⁹, hydrogen embrittlement ³, or mechanical failure ¹⁰.

Grain boundaries (GBs) are among the most important features of the microstructure, occupying an area of 500-1,000 football fields per cubic meter material with 1 μm grain size. On the one hand, they render positive effects such as the simultaneous increase in strength and ductility ^{11,12}, but on the other hand they make materials vulnerable, for crack initiation ¹⁰, onset of corrosion ⁹, pinning of magnetic domain walls ¹³, diffusional intrusion¹⁴ or reduction in electrical conductivity ¹⁵. These features qualify GBs as the most important microstructural defects for many high-performance materials.

Two key factors are missing in our knowledge about GBs. The first one is the systematic and meaningful representation of GBs with pertinent and property-oriented parameters: their characterization requires five geometric degrees of freedom ¹⁶ and further parameters to describe them down to their atomistic-scale facets ¹⁷⁻²¹ and motifs ²²⁻²⁶, yet, it is still elusive which of these really matter for structure-property relations. By motifs we mean here certain geometric polyhedra built by atoms that form repeating units to constitute the GBs ^{5,23-27}, e.g., the kite ^{24,28}, domino, and pearl ^{22,29} structures that were described before to decipher the GB's elementary 'genetic' structure. This concept of the GB motif was inspired by the early works of Gaskell ^{30,31} and Bernal ³²: they described liquids and amorphous materials as an arrangement of polyhedral structural atomic units and found that only a surprisingly small number of them is needed to construct such complex materials. Identifying key properties of GBs across all these scales at systematic variation of these parameters has not yet been realized. The second one is the difficulty of characterizing both, the GB structure (in all these aspects) and their chemical decoration state down to the atomic scale.

The hierarchy of the GB structure across these different features is complex: an adequate representation of a GB at least requires to define the misorientation between adjacent grains and the inclination of the GB plane. At a mesoscopic view energy-favored GB planes are normally the most densely packed ones which comprise a high density of atomic coincidence sites, derived from a virtual lattice that extends over both adjacent crystals (CSL) ³³. At a refined scale it is found that the GB planes do not generally follow this geometrical criterion alone but that they can further decompose into a sequence of piecewise planar facets, which are sets of reconstruction motifs of lower total energy ^{18,28}. At the atomic level, local GB structures, including the faceting ^{18,19,28}, as well as many other features such as secondary defects³⁴, ordering ^{2,35-38} and phase transformation ^{22,39,40}, can play crucial roles in the spatial distribution of solute atoms within GB planes. This complex interplay between GB structure and chemistry leads to a deviation from the Langmuir-

McLean type of (sub-)monolayer adsorption behavior¹⁶, which takes a thermodynamic view at chemical decoration, yet, is structurally agnostic to these fine atomic details. This complexity shows that – in order to gain a fundamental understanding of the coupling behavior between structure and chemical composition – direct experimental observation of all these structure features and across all these scales, together with a mapping of the GBs chemical composition is required. This must be done under conditions, where each of these parameters is varied systematically, step-by-step, while the other parameters are kept constant.

For this study, we have developed a custom-designed workflow along an instrument ensemble which allows to map the structure, chemistry and electronic state of GBs at length scales ranging from macroscopic to atomic. The macro- and mesoscale study of GB structure was carried out by optical, scanning electron microscopy (SEM), and diffraction imaging. We observed atomic GB structures using probe-corrected high angle annular dark field - scanning transmission electron microscopy (HAADF-STEM)^{6,22}. We used atom probe tomography (APT)⁴¹ to quantify the distribution of solutes along the GB plane at the nanoscale⁴²⁻⁴⁵. APT has the sensitivity to detect all elements in the periodic table, and provides 3D chemical composition using machine-learning enhanced mapping⁴⁶ of the chemical decoration inside the GB planes, routinely for areas as large as 10,000 nm². Direct imaging of the atomic structure at GBs is currently not possible for APT due to the limited spatial resolution of approximately 0.1-0.3 nm in depth and 0.3-0.5 nm in width^{47,48}, and the local magnification effect⁴⁹⁻⁵¹. We used differential phase contrast – four dimensional STEM (DPC-4DSTEM) to map low atomic number objects and the local charge-density of crystalline materials with sub-Ångström resolution⁵²⁻⁵⁸. We reconstructed the charge-density maps from the DPC-4DSTEM data to spatially resolve B and C atoms decorating the Fe GBs.

With this multi-scale and multi-physics GB analysis approach we make the surprising observation that it is actually not the macroscopic or mesoscopic geometrical aspects that explain the specific chemical decoration state of an interface as is usually claimed. Instead, features at the smallest length scales, i.e. the atomistic motifs, determine the chemistry of a GB. As a model material we have chosen a Bridgeman-produced body-centered cubic (bcc) – Fe $\Sigma 5$ (where $\Sigma 5$ is the density of coincident sites³³) bicrystal, stabilized by approximately 4 at.% Al and alloyed with C and B atoms⁶. We have selected this material as Fe-C alloys, also referred to as steels, represent about 1.9 billion tons of material produced each year⁷, by far the most common metal class, with an uncounted number of safety critical and functional applications, ranging from huge infrastructure to tiny magnets. B has been selected as a second alloy element owing to its peculiar, and often highly beneficial effect on GB cohesion and the resulting material properties¹¹.

Hierarchical characterization of grain boundaries

We grew bcc - Fe $\Sigma 5$ bicrystals⁶. During the growth process, the GB plane changed its orientation with respect to the neighboring grains, see the orange dashed line superimposed on the optical image in Fig. 1a. We cut a disk (5 mm thick and 2 cm in diameter, marked as a blue rectangle in Fig. 1a) from the bicrystals to investigate the hierarchical structure and composition of the GB over 9 orders of magnitude in size scale using a variety of characterization methods (see Fig. 1). Macroscopically, this particular region exhibits a significant change in the GB plane inclination perpendicular to the growth direction, but remains relatively straight along the growth direction, see the optical image in Fig. 1a.

Fig. 1b shows the mesoscale GB character measured by electron backscatter diffraction (EBSD). The GB has a total length of approximately 1 cm. We divided the GB into regions of interest (ROIs) from #1 to #91 with 10 μm horizontal distance between each number. The orientation of the adjacent grains remained constant, while the GB plane systematically changed its angle, see the inset blue cubes and yellow lines. We quantified the rotation of the GB planes by the inclination, which is the angle between the GB plane and the inner bisector between the [010] directions in the grains. The inclination changed from 0° to 60° with a monotonic variation (see Fig. 1b, more measurements are referred to Extended Data Fig. 1).

At the nano- and atomic scales, we found that GBs are not flat. Faceting, discontinuities, and steps occur at a high number density along the GB plane. For example, the 4DSTEM orientation map and the HAADF-STEM image in Fig. 1c show facet structures along the $\Sigma 5$ [430]//[010] GB. Such abrupt local structural variation leads to a dramatic change in the spatial distribution of solute atoms within the GB planes, showing that it is not the mesoscopic alignment but the atomic-scale motif- and facet-structure which determines its chemical decoration. Fig. 1d shows a representative APT measurement of the same $\Sigma 5$ [430]//[010] GB, where the local content of C and B varies significantly along the curved GB plane. We present more 4DSTEM orientation maps in Extended Data Fig. 2 and APT reconstructions in Extended Data Fig. 3.

We observed the light B and C atomic columns at the local GB motifs using the recently developed DPC-4DSTEM imaging technique^{53,54,58}. As shown in Fig. 1e, the atomic columns containing the B or C atoms at $\Sigma 5$ (310) // ($3\bar{1}0$) GB were revealed and validated by a combination of experimental and simulated charge-density maps reconstructed from the DPC-4DSTEM data sets. The contrast for the light atoms, here B or C, is weak in the dark-field image due to their much lower atomic weight compared to Fe. Using the charge-density maps, we were able to detect a clear signal in the center of the GB atomic motif structure (referred to as 'kite'^{24,28}), representing the B or C-containing atomic columns. The charge density map can also provide an opportunity to study the electronic structure of the GB⁵⁴. Here light atoms in the Fe GB have been directly imaged in the electron microscope at sub-Ångström- resolution.

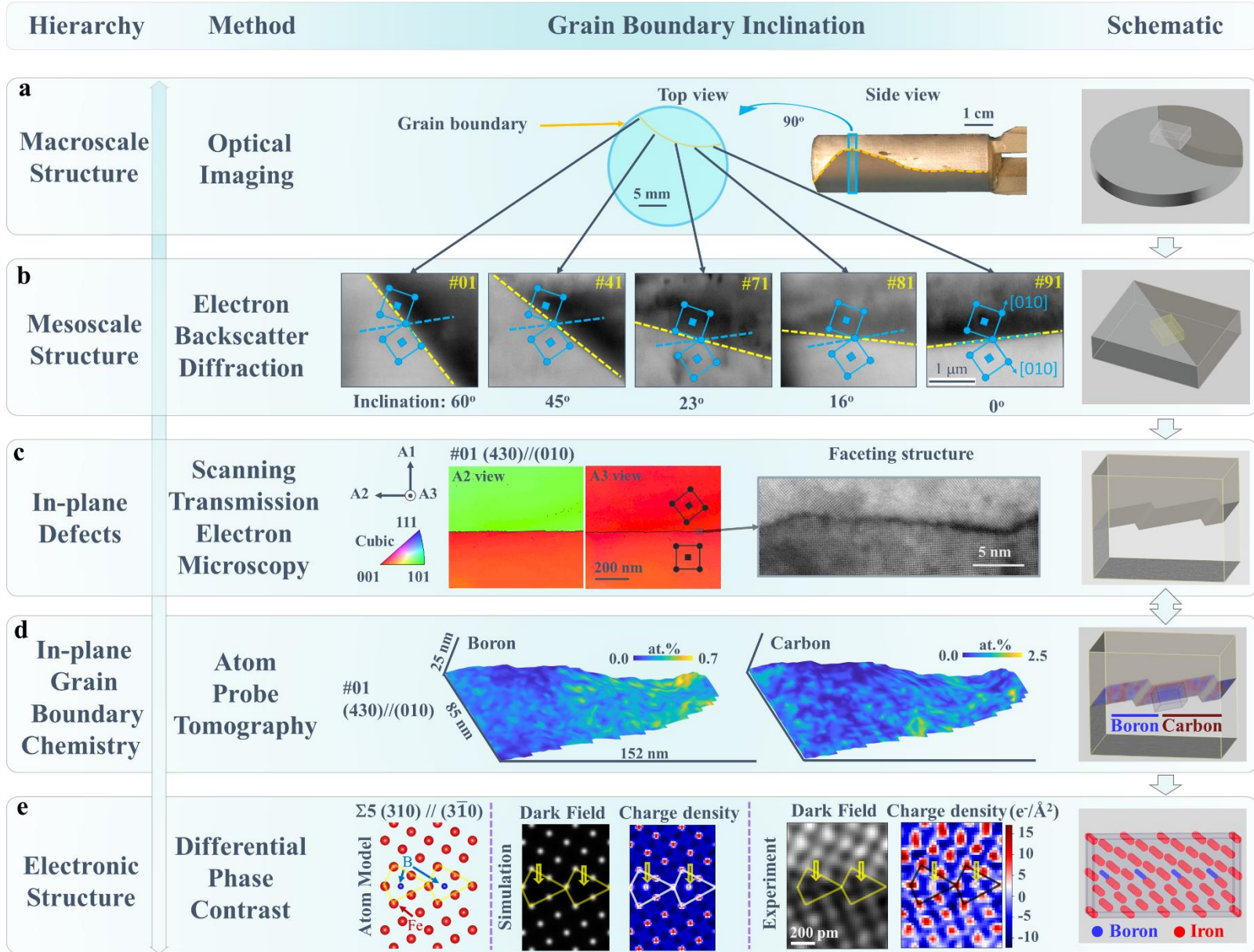


Fig. 1 Hierarchy study of $\Sigma 5$ Fe grain boundaries (GBs) over 9 orders of magnitude. **a** Macroscale information of the $\Sigma 5$ bicrystals. **b** Structural characterization of $\Sigma 5$ GBs at mesoscale level by electron backscatter diffraction (EBSD). A continuous change in the inclination of the GB was recorded while the misorientation between the adjacent grains remained constant. The number indicates the position at which the EBSD scan was acquired, ranging from #1 - # 91, at 10 μm spacing, see the illustration in a. The blue squares represent the body-centered cubic (bcc) unit cells imaged at [001] direction. **c** shows in-plane defects in the representative $\Sigma 5$ (430) // (010) GB. The two left hand side images show the reconstruction of the orientation from the four-dimensional scanning transmission electron microscopy (4DSTEM) data set. The black squares represent the body-centered cubic (bcc) unit cells imaged at [001] direction. The right image is the high angle annular dark field (HAADF) – scanning transmission electron microscopy (STEM) image. **d** The local composition of B and C along the $\Sigma 5$ (430) // (010) GB plane. **e** Imaging light B and C atoms in the center of the kite structure for a $\Sigma 5$ (310) // ($3\bar{1}0$) GB using differential phase contrast (DPC)-4DSTEM imaging. The left image shows the atomic model structure of the $\Sigma 5$ Fe (colored in red) GB with B (blue) decoration. The right image includes the reconstructed dark-field and charge-density map for both simulated and experimental data sets. The last column of each row shows the schematic illustration of the main structural features of a given hierarchy.

Grain boundary chemistry

We have systematically quantified the GB chemistry for a series of $\Sigma 5$ -GBs with different inclinations using APT. The analyses include two symmetric GBs, #41 $\Sigma 5$ (310) // ($3\bar{1}0$) GB and #91 $\Sigma 5$ ($2\bar{1}0$) // ($1\bar{2}0$) GB, as well as two asymmetric GBs, #01 $\Sigma 5$ (430) // (010) GB and #71 $\Sigma 5$ (11 1 0) // ($9\bar{8}0$). To better understand the influence of the GB inclination on their chemical properties, we selected ROIs in which the GBs appeared to be flat in the reconstructed APT volume. For example, Fig. 2a shows the atom maps of Fe, B, and C, extracted from a region with a $\Sigma 5$ (310) // ($3\bar{1}0$) GB. We found a clear tendency for B and C to segregate at the GB, which is consistent with previous theoretical and experimental studies^{6,59-65}. It is worth noting that the detailed study of Al depletion caused by the co-segregation of B and C was reported in our previous publication⁶. In the current work, we focus on the segregation behavior of the light elements B and C.

We quantified the in-plane solute compositions of B and C throughout the GB. The composition ranges for B and C are 0.2-1.3 atomic (at.) % and 0.2-1.7 at. %, respectively, corresponding to interfacial excesses of 0.7-4.5 atoms (at.)/ nm^2 and 0-5.7 atom(at.)/ nm^2 , respectively. In a GB composed of kite structures, the center of a single kite structure includes several sites in the direction perpendicular to the projection

direction of the kite structure; these sites may be fully or partially occupied by interstitial atoms, resulting in different solute content, i.e., different values of interfacial excess. When the center of the kite structure consisting of a $\Sigma 5$ (310) // (3 $\bar{1}$ 0) GB is fully occupied by interstitial atoms, the interfacial excess is 7.7 at./nm². According to our APT results, there is less than a monolayer adsorption of B or C atoms at this $\Sigma 5$ (310) // (3 $\bar{1}$ 0) GB, since the interfacial excesses for both B and C are less than 7.7 at./nm². The mean occupancies for B and C are approximately 31% and 38%, respectively.

We also noticed an inhomogeneous segregation pattern of both B and C in the contour maps of their compositions in the GB planes⁴⁶ (see Fig. 2b). First, it must be clarified that due to the limited detection rate and trajectory aberration^{41,66}, APT cannot provide a reconstruction in which every atom in the bulk material is accurately reconstructed. Here for the spatially resolved solute content along the GB plane, the quantification results represent the statistics over several, approximately 10-20, kite structures. The solute content values in Fig. 2b do not show the composition of each individual kite structure, but the average value for several kite structures. Although the composition of each kite provides more information about the physical interrelationships from the energy point of view. It is not possible to directly learn the atomic level information from the APT measurements. However, the statistics of an average value can readily provide a general understanding of the behavior of solute-solute interaction at GBs^{42,67}.

Interestingly, the decoration with B and C are not strongly correlated but some regions appears to be mutually repulsive, i.e., regions enriched in B can have a low content of C (see Fig. 2b) and vice versa. We quantified the Pearson product-moment correlation coefficient between the local GB compositions of B and C as 0.02, which is midway between the lower (-1, anti-correlated) and upper (1, perfect correlation) bounds, indicating a very weak correlation. There are two main reasons for the inhomogeneous segregation. The first reason is composition-dependent segregation behavior^{6,68}. In our previous work, we used density functional theory (DFT) to study this phenomenon and we found that increased coverage of interstitial or substitutional sites, e.g. by B and C, decreases the segregation tendency, suggesting that co-segregation effects limit the enrichment of B and C⁶. More specifically, the segregation energy for B at the interstitial sites is -2.6 eV - -2.8 eV, indicating a strong segregation tendency. However, when additional B or C is present at the second nearest (to GB) interstitial sites, the segregation energy for interstitial sites approaches zero or even reaches positive values. In these cases, further segregation is energetically unfavorable⁶.

The second reason is site- and motif-specific segregation, which is determined by the local GB motifs in the GB plane^{19,62}. Wang et al.⁶² found that more open GB structures, e.g., with local motifs such as $\Sigma 5$ (310) // (3 $\bar{1}$ 0) or $\Sigma 5$ (2 $\bar{1}$ 0) // (1 $\bar{2}$ 0), are energetically more favorable for C segregation compared to more compact structure units, such as e.g. the local motif $\Sigma 3$ (2 $\bar{1}$ 1) // (1 $\bar{2}$ 1). For a GB with the same CSL value, e.g., a $\Sigma 5$ GB, the segregation energies for C at the interstitial site reduced from -1.13 eV/atom to -1.40

eV/atom when the GB motif changes from $\Sigma 5 (310) // (3\bar{1}0)$ to $\Sigma 5 (2\bar{1}0) // (1\bar{2}0)$ at full coverage⁶². This finding shows that the local $\Sigma 5 (2\bar{1}0) // (1\bar{2}0)$ motif is energetically more favorable for C segregation than the $\Sigma 5 (310) // (3\bar{1}0)$ motif. The GB motif-dependent segregation tendency has also been reported for the system Cu-Ag by Peter et al.¹⁹, where nanometer-sized facets were observed to be composed of preferentially Ag-segregated symmetric $\Sigma 5\{210\} // \{210\}$ segments and Ag-depleted $\{230\} // \{100\}$ asymmetric segments. In our study, the inhomogeneous B and C segregation is therefore attributed to the changes in these local motifs. In the following sections, we will address the atomic structure of the different local motifs in more detail.

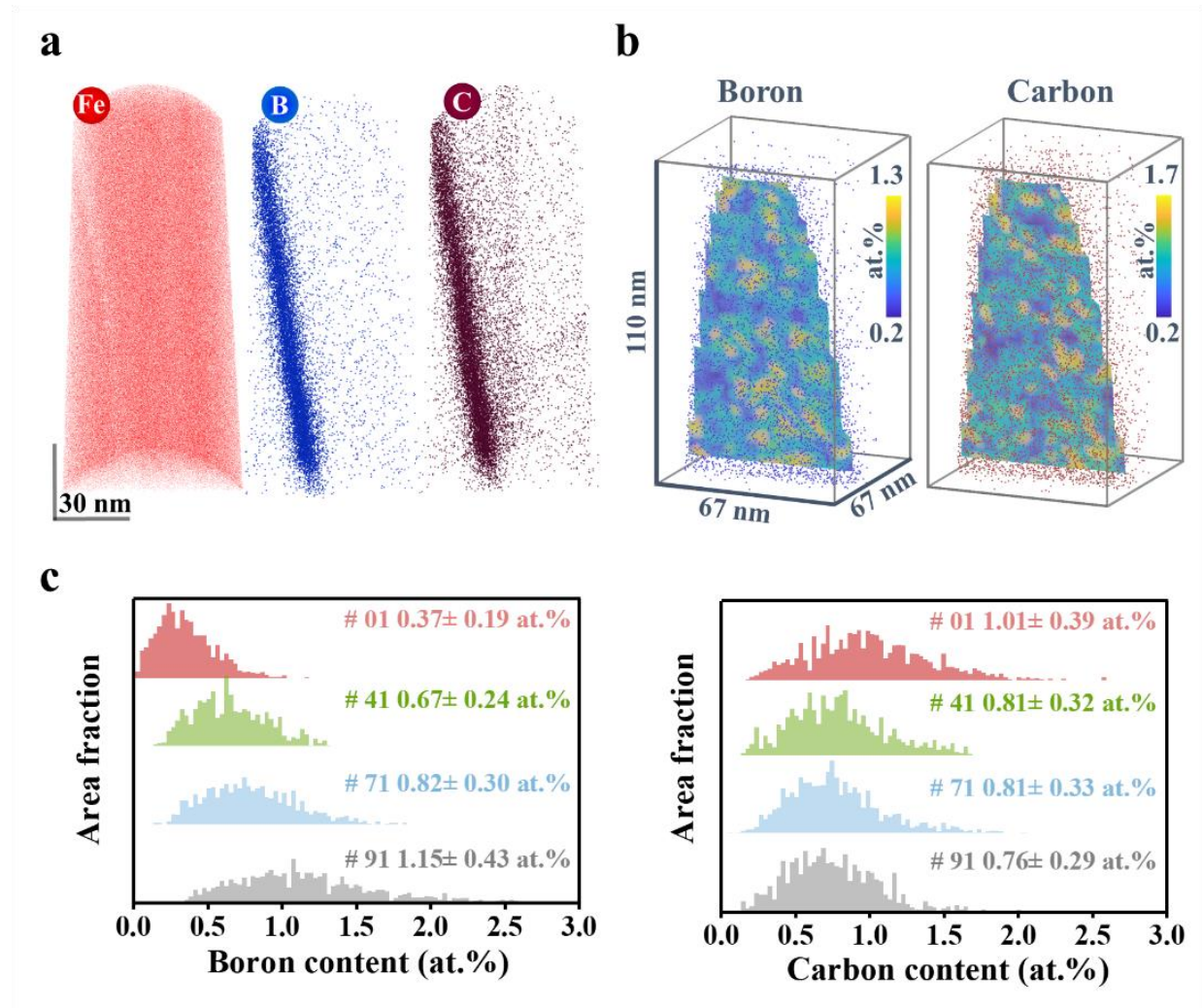


Fig. 2 Local chemical composition analysis for $\Sigma 5$ GBs. **a** Fe (only show 3 at. % of total Fe atoms), B, and C atom maps from the atom probe tomography (APT) reconstruction of the $\Sigma 5 (310) // (3\bar{1}0)$ GB. **b** Contour maps of the solute B and C compositions along the GB planes shown in **a**. **c** The distribution of B and C atoms along the GB planes of #01 $\Sigma 5 (430) // (010)$, #41 $\Sigma 5 (310) // (3\bar{1}0)$, #71 $\Sigma 5 (11\bar{1}0) // (9\bar{8}0)$

and #91 $\Sigma 5$ $(2\bar{1}0) // (1\bar{2}0)$ GBs, represented by the area fraction of a given B or C content as a function of B or C composition.

Additional in-plane quantitative GB chemistry results are summarized in Fig. 2c (see each of the APT reconstruction in the Extended Data in Fig. 3). The average B content increased from 0.37 ± 0.19 at. % to 1.15 ± 0.43 at. % as the GB inclination decreased from 60° for $\Sigma 5$ $(310) // (3\bar{1}0)$ to 0° for $\Sigma 5$ $(2\bar{1}0) // (1\bar{2}0)$. The B segregation at the $\Sigma 5$ $(2\bar{1}0) // (1\bar{2}0)$ GB is approximately twice that at the $\Sigma 5$ $(310) // (3\bar{1}0)$ GB and more than three times that at the $\Sigma 5$ $(430) // (010)$ GB. For the average in-plane composition of C, a relatively constant composition of 0.8 at. % was observed for GBs with different inclinations, except for the $\Sigma 5$ $(430) // (010)$ GB, which is about 25% higher than for the other GBs. Summarizing the segregation of B and C, a maximum solute content of 1.95 at% is observed for the $\Sigma 5$ $(2\bar{1}0) // (1\bar{2}0)$ GB. $\Sigma 5$ $(310) // (3\bar{1}0)$ GB and $\Sigma 5$ $(430) // (010)$ GB have a relatively low solute content of approximately 1.4 at%, see Extended Data Fig. 4. Our APT observation is consistent with the theoretical prediction of Wang et al.⁶².

Facet structures

Fig. 3 shows selected HAADF-STEM images for the four representative GBs we studied for the in-plane GB chemistry. More images of these GBs can be found in the Extended Data Fig. 5. We have drawn yellow lines to highlight the projection of GB planes where atomically sharp GBs were detected. This indicates that the lamellae samples are so thin that the inclination of the GBs in the projection direction is not pronounced, i.e., the structures are essentially constant along the projection direction.

Fig. 3a shows the $\Sigma 5$ $(430) // (010)$ GB in which in-plane defects occur continuously to compensate for the lattice mismatch between the (110) and (010) planes among the adjacent grains. The $\Sigma 5$ $(310) // (3\bar{1}0)$ GB appears relatively straight, with the local GB motifs showing the typical kite structure, Fig. 3b. In this GB, a step connecting two regions with kite structure was observed. For the $\Sigma 5$ $(11\ 1\ 0) // (9\bar{8}0)$ GB in Fig. 3c, we found a nanofacet morphology with different combinations between local motifs, such as $\Sigma 5$ $(310) // (3\bar{1}0)$, $\Sigma 5$ $(2\bar{1}0) // (1\bar{2}0)$, $\Sigma 5$ $(010) // (1\bar{1}0)$, etc. In the last case, the $\Sigma 5$ $(2\bar{1}0) // (1\bar{2}0)$ GB shown in Fig. 3d, the majority of GB motifs are the straight $\Sigma 5$ $(2\bar{1}0) // (1\bar{2}0)$ GB with the intervening $\Sigma 5$ $(010) // (1\bar{1}0)$ facet. We tabulated all observed local GB motifs in Fig. 3e, where three local GB motifs dominate: $\Sigma 5$ $\{110\} // \{010\}$, $\Sigma 5$ $\{310\} // \{310\}$, and $\Sigma 5$ $\{210\} // \{120\}$, which are highlighted in yellow, magenta, and green, respectively. Here, for the symmetric $\Sigma 5$ GB motifs, including $\Sigma 5$ $\{310\} // \{310\}$ and $\Sigma 5$ $\{210\} // \{120\}$,

the kite-shaped structural units are commonly identified and also predicted from DFT and Mendeleev calculations^{28,59,68,69}. However, there are less reports on the asymmetric $\Sigma 5$ $\{110\} // \{010\}$ GB motifs.

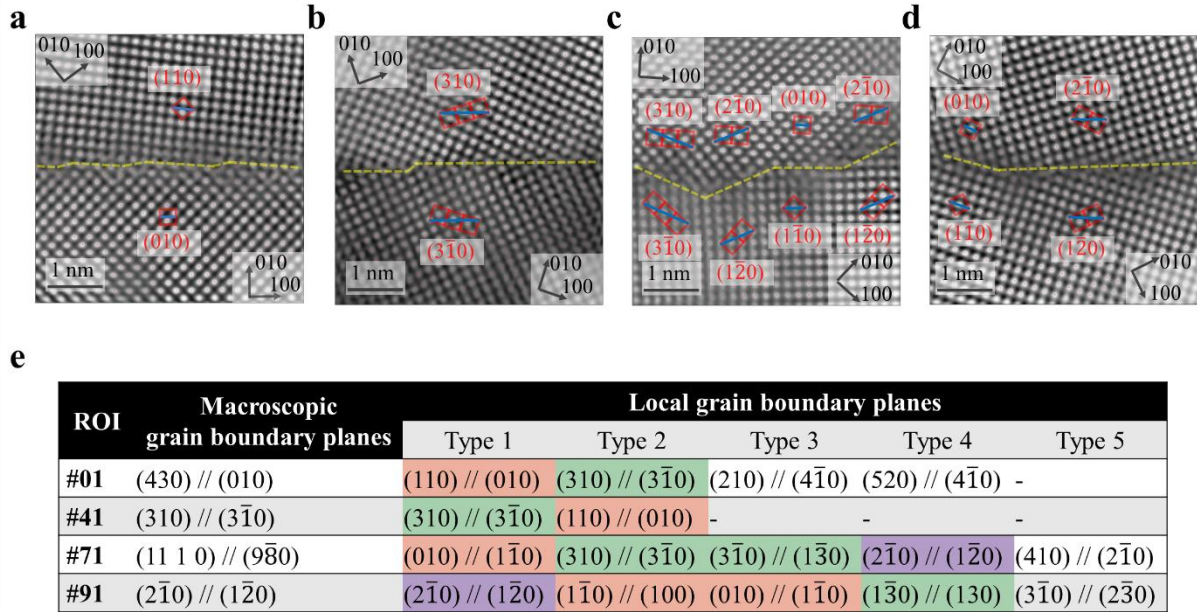


Fig. 3 HAADF-STEM images of the local GB structures. a-d are $\Sigma 5$ GBs with the local plane pairs (430) // (010), (310) // (3̄10), (11 1 0) // (9̄80) and (2̄10) // (1̄20), respectively. The yellow lines indicate the positions of the GBs. The red squares and blue lines assist in identifying the local GB planes. e Summary table showing the local GB planes for $\Sigma 5$ GBs with different macroscopic GB inclinations.

Imaging light B and C atoms at grain boundaries

We have next studied the above mentioned three types of prevalent atomic GB motifs with regards to the occurrence of the light elements B and C, using the DPC-4DSTEM method. B and C atomic columns are identified by locating peaks with weak or no contrast in the dark-field images, but strong contrast in the charge density maps. The full reconstruction, including the electric field, the (projected) electrostatic potential, and the charge-density maps, can be found in the Extended Data Fig. 6. Fig. 4 shows only the reconstructed dark-field image (top row) and the charge-density map (bottom row) for each GB motif. More ROIs of the local GB motifs can be found in the Extended Data Fig. 7.

In Fig. 4a, we highlighted the $\Sigma 5$ (110) // (010) motif with a yellow triangle. The B and C atomic columns are marked with black arrows in the charge-density map, which appear far apart, indicating a potentially low solute content in this GB type. Fig. 4b shows the typical kite structure of the $\Sigma 5$ (310) // (3̄10) motif,

highlighted by yellow quads. In the charge-density map, we found that the center of the kite structure is occupied by light atoms. It is worth noting that this DPC-4DSTEM method can only detect whether there is an atomic column consisting of light elements but it cannot distinguish what type of solute it is, i.e. whether it is a predominantly B or C-occupied atomic column or a mixed state (see Extended Data Fig. 8). Based on our preliminary DFT study, all of these occupation states have been shown to be energetically favorable⁶. The last $\Sigma 5$ ($2\bar{1}0$) // ($1\bar{2}0$) motif is more complicated, as we identified two different variants of this type. Fig. 4c shows one variant of the motif, which appears to be a separated kite structure, as highlighted with yellow quads and a line. Similar to the $\Sigma 5$ (310) // ($3\bar{1}0$) motif, the B or C atomic columns can also occupy the center of the kite structure. Another variant of this motif for the $\Sigma 5$ ($2\bar{1}0$) // ($1\bar{2}0$) type structure is the extended kite structure, see Extended Data Fig. 7c iii-vi. We found that this type of motif variant is commonly more distorted^{6,62,63,68}, which might be a reason that it can accommodate higher fractions of interstitial or substitutional sites that are suited for hosting B or C. This result is consistent with the quantifications from our APT results, see Fig. 2c, where the composition of solutes for the $\Sigma 5$ ($2\bar{1}0$) // ($1\bar{2}0$) GB shows a wide range and its mean composition is the highest of all GBs studied, up to 1.95 at% for total B and C content. The theoretical prediction of Wang et al.⁶² also suggests that the $\Sigma 5$ ($2\bar{1}0$) // ($1\bar{2}0$) type structure is energetically more favorable for the interstitial segregation of C than the $\Sigma 5$ (310) // ($3\bar{1}0$) type structure. This direct atomic-scale observation of the motif structures underneath the mesoscale plane inclination features provides an explanation for the profound differences among GBs with different inclinations for their chemical decoration states observed by APT.

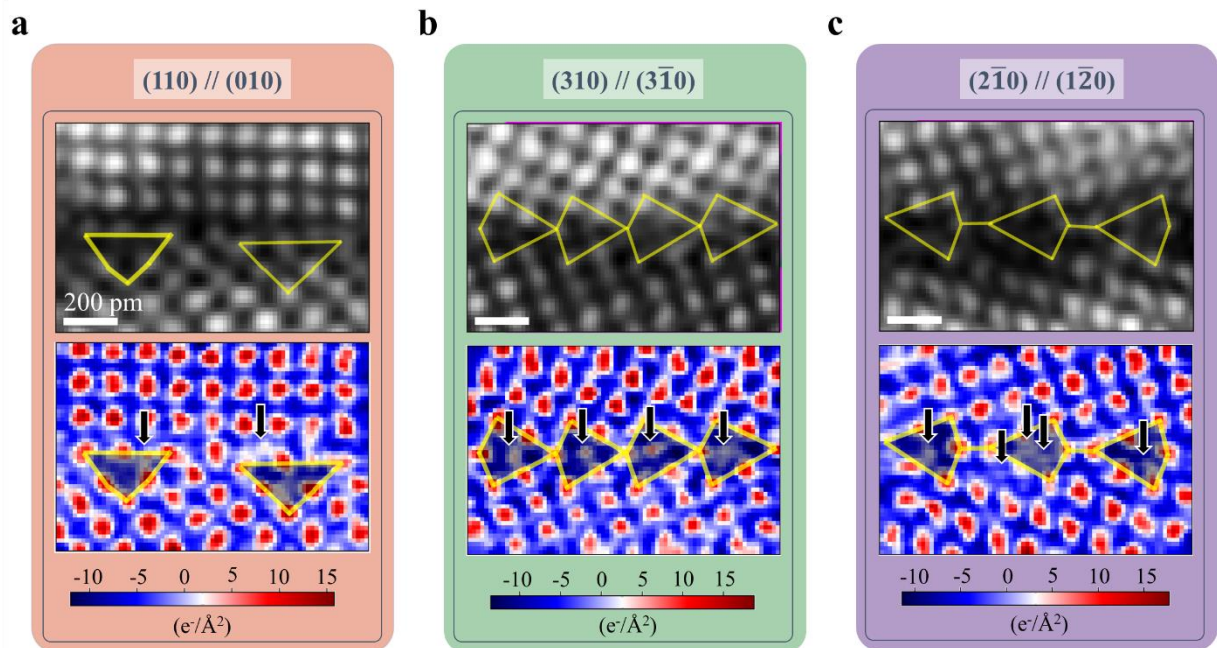


Fig. 4 B and C atoms at $\Sigma 5$ GBs. Three representative local GB motifs: **a** $\Sigma 5$ (110) // (010); **b** $\Sigma 5$ (310) // ($3\bar{1}0$); **c** $\Sigma 5$ ($2\bar{1}0$) // ($1\bar{2}0$). For each local GB motif, the dark-field and charge-density map reconstructed from the atomic DPC-4DSTEM data sets are shown in the top and bottom panels, respectively. The repeated structures are highlighted in yellow lines in the dark-field map. The B or C atomic columns are indicated by black arrows in the charge-density maps.

In summary, we performed a holistic, multiscale analysis of the hierarchical, structural, and chemical features of GBs using high-resolution imaging techniques including HAADF-STEM, APT, and atomic DPC-4DSTEM, which extends over 9 orders of magnitude in spatial resolution. We find that the chemical properties of GBs cannot be simply determined by their CSL value or mesoscopic angular features alone, but instead strongly depend on their GB inclination, the resulting faceting, and particularly on the local atomic motifs. Using charge-density maps, we were able to directly map the atomic columns of light elements B and C in the GBs of an Fe bicrystal. These results not only yield direct experimental evidence for understanding the chemical nature of GBs on the basis of their atomic-scale structural properties, but also provide the scientific basis for developing advanced materials with controllable interfaces.

References

- 1 Wu, R. Q., Freeman, A. J. & Olson, G. B. First Principles Determination of the Effects of Phosphorus and Boron on Iron Grain-Boundary Cohesion. *Science* **265**, 376-380, doi:10.1126/science.265.5170.376 (1994).
- 2 Luo, J., Cheng, H. K., Asl, K. M., Kiely, C. J. & Harmer, M. P. The Role of a Bilayer Interfacial Phase on Liquid Metal Embrittlement. *Science* **333**, 1730-1733, doi:10.1126/science.1208774 (2011).
- 3 Zhao, H. *et al.* Hydrogen trapping and embrittlement in high-strength Al alloys. *Nature* **602**, 437-441, doi:10.1038/s41586-021-04343-z (2022).
- 4 Sorby, H. C. On the microscopical structure of iron and steel. *The Journal of Iron and Steel* **1**, 255-289 (1887).
- 5 Sutton, A. P. On the structural unit model of grain boundary structure. *Philosophical Magazine Letters* **59**, 53-59, doi:10.1080/09500838908214777 (1989).
- 6 Ahmadian, A. *et al.* Aluminum depletion induced by co-segregation of carbon and boron in a bcc-iron grain boundary. *Nat. Commun.* **12**, 6008, doi:10.1038/s41467-021-26197-9 (2021).
- 7 Raabe, D., Tasan, C. C. & Olivetti, E. A. Strategies for improving the sustainability of structural metals. *Nature* **575**, 64-74, doi:10.1038/s41586-019-1702-5 (2019).
- 8 Mori, H., Asami, K. & Ohtsuka, Y. Role of Iron Catalyst in Fate of Fuel Nitrogen during Coal Pyrolysis. *Energy & Fuels* **10**, 1022-1027, doi:10.1021/ef960035d (1996).
- 9 King, A., Johnson, G., Engelberg, D., Ludwig, W. & Marrow, J. Observations of Intergranular Stress Corrosion Cracking in a Grain-Mapped Polycrystal. *Science* **321**, 382-385, doi:10.1126/science.1156211 (2008).

- 10 Kondo, S., Ishihara, A., Tochigi, E., Shibata, N. & Ikuhara, Y. Direct observation of atomic-scale fracture path within ceramic grain boundary core. *Nat. Commun.* **10**, 2112, doi:10.1038/s41467-019-10183-3 (2019).
- 11 Kuzmina, M., Ponge, D. & Raabe, D. Grain boundary segregation engineering and austenite reversion turn embrittlement into toughness: Example of a 9wt.% medium Mn steel. *Acta Mater* **86**, 182-192, doi:<https://doi.org/10.1016/j.actamat.2014.12.021> (2015).
- 12 Raabe, D. *et al.* Segregation engineering enables nanoscale martensite to austenite phase transformation at grain boundaries: A pathway to ductile martensite. *Acta Mater* **61**, 6132-6152, doi:10.1016/j.actamat.2013.06.055 (2013).
- 13 Marincel, D. M. *et al.* Influence of a Single Grain Boundary on Domain Wall Motion in Ferroelectrics. *Adv. Funct. Mater.* **24**, 4205-4205, doi:<https://doi.org/10.1002/adfm.201401578> (2014).
- 14 Kitaguchi, H. S. *et al.* An atom probe tomography study of the oxide-metal interface of an oxide intrusion ahead of a crack in a polycrystalline Ni-based superalloy. *Scr. Mater.* **97**, 41-44, doi:<https://doi.org/10.1016/j.scriptamat.2014.10.025> (2015).
- 15 Braunovic, M. & Haworth, C. W. Grain - Boundary Contribution to the Electrical Resistivity of Iron. *J. Appl. Phys.* **40**, 3459-3464, doi:10.1063/1.1658219 (1969).
- 16 Lejcek, P. *Grain Boundary Segregation in Metals*. Vol. 136 (Springer, 2010).
- 17 Zhao, H. *et al.* Interplay of Chemistry and Faceting at Grain Boundaries in a Model Al Alloy. *Phys. Rev. Lett.* **124**, 106102, doi:10.1103/PhysRevLett.124.106102 (2020).
- 18 Abdeljawad, F., Medlin, D. L., Zimmerman, J. A., Hattar, K. & Foiles, S. M. A diffuse interface model of grain boundary faceting. *J. Appl. Phys.* **119**, 235306, doi:<https://doi.org/10.1063/1.4954066> (2016).
- 19 Peter, N. J. *et al.* Segregation-Induced Nanofaceting Transition at an Asymmetric Tilt Grain Boundary in Copper. *Phys. Rev. Lett.* **121**, 255502, doi:10.1103/PhysRevLett.121.255502 (2018).
- 20 Liebscher, C. H. *et al.* Strain-Induced Asymmetric Line Segregation at Faceted Si Grain Boundaries. *Phys. Rev. Lett.* **121**, 015702, doi:10.1103/PhysRevLett.121.015702 (2018).
- 21 Priedeman, J. L. & Thompson, G. B. The influence of alloying in stabilizing a faceted grain boundary structure. *Acta Mater* **201**, 329-340, doi:<https://doi.org/10.1016/j.actamat.2020.09.085> (2020).
- 22 Meiners, T., Frolov, T., Rudd, R. E., Dehm, G. & Liebscher, C. H. Observations of grain-boundary phase transformations in an elemental metal. *Nature* **579**, 375-378, doi:10.1038/s41586-020-2082-6 (2020).
- 23 Ashby, M. F., Spaepen, F. & Williams, S. The structure of grain boundaries described as a packing of polyhedra. *Acta Metall.* **26**, 1647-1663, doi:[https://doi.org/10.1016/0001-6160\(78\)90075-5](https://doi.org/10.1016/0001-6160(78)90075-5) (1978).
- 24 Sutton, A. P., Vitek, V. & Christian, J. W. On the structure of tilt grain boundaries in cubic metals I. Symmetrical tilt boundaries. *Philosophical Transactions of the Royal Society of London. Series A, Mathematical and Physical Sciences* **309**, 1-36, doi:10.1098/rsta.1983.0020 (1983).
- 25 Sutton, A. P. & Vitek, V. On the Structure of Tilt Grain Boundaries in Cubic Metals II. Asymmetrical Tilt Boundaries. *Philosophical Transactions of the Royal Society of London. Series A, Mathematical and Physical Sciences* **309**, 37-54, doi:<https://doi.org/10.1098/rsta.1983.0020> (1983).
- 26 Banadaki, A. D. & Patala, S. A three-dimensional polyhedral unit model for grain boundary structure in fcc metals. *npj Computational Materials* **3**, 13, doi:10.1038/s41524-017-0016-0 (2017).
- 27 Balluffi, R. W. Grain boundary diffusion mechanisms in metals. *Metallurgical Transactions B* **13**, 527-553, doi:10.1007/BF02650011 (1982).
- 28 Medlin, D. L., Hattar, K., Zimmerman, J. A., Abdeljawad, F. & Foiles, S. M. Defect character at grain boundary facet junctions: Analysis of an asymmetric Sigma=5 grain boundary in Fe. *Acta Mater* **124**, 383-396, doi:10.1016/j.actamat.2016.11.017 (2017).

- 29 Frommeyer, L. *et al.* Dual phase patterning during a congruent grain boundary phase transition in elemental copper. *Nat. Commun.* **13**, 3331, doi:10.1038/s41467-022-30922-3 (2022).
- 30 Gaskell, P. H. A new structural model for transition metal–metalloid glasses. *Nature* **276**, 484–485, doi:10.1038/276484a0 (1978).
- 31 Gaskell, P. H., Smith, D. J., Catto, C. J. D. & Cleaver, J. R. A. Direct observation of the structure of a metallic alloy glass. *Nature* **281**, 465–467, doi:10.1038/281465a0 (1979).
- 32 Bernal, J. D. A Geometrical Approach to the Structure Of Liquids. *Nature* **183**, 141–147, doi:10.1038/183141a0 (1959).
- 33 Ranganathan, S. On the Geometry of Coincidence-Site Lattices. *Acta Crystallographica Section A* **21**, 197–199, doi:<https://doi.org/10.1107/S0365110X66002615> (1966).
- 34 Han, J., Thomas, S. L. & Srolovitz, D. J. Grain-boundary kinetics: A unified approach. *Prog. Mater. Sci.* **98**, 386–476, doi:<https://doi.org/10.1016/j.pmatsci.2018.05.004> (2018).
- 35 Xie, H. *et al.* Twin Boundary Superstructures Assembled by Periodic Segregation of Solute Atoms. *Nano Letters*, 1c03448, doi:10.1021/acs.nanolett.1c03448 (2021).
- 36 Nie, J. F., Zhu, Y., Liu, J. & Fang, X.-Y. Periodic segregation of solute atoms in fully coherent twin boundaries. *Science* **340**, 957–960, doi:10.1126/science.1229 (2013).
- 37 Yu, Z. *et al.* Segregation-induced ordered superstructures at general grain boundaries in a nickel–bismuth alloy. *Science* **358**, 97–101, doi:10.1126/science.aam8256 (2017).
- 38 Wang, Z. *et al.* Atom-resolved imaging of ordered defect superstructures at individual grain boundaries. *Nature* **479**, 380–383, doi:10.1038/nature10593 (2011).
- 39 Frolov, T., Olmsted, D. L., Asta, M. & Mishin, Y. Structural phase transformations in metallic grain boundaries. *Nat. Commun.* **4**, 1038, doi:<https://doi.org/10.1038/ncomms2919> (2013).
- 40 Cantwell, P. R. *et al.* Grain Boundary Complexion Transitions. *Annu. Rev. Mater. Res.* **50**, 465–492, doi:10.1146/annurev-matsci-081619-114055 (2020).
- 41 Gault, B. *et al.* Atom probe tomography. *Nature Reviews Methods Primers* **1**, 51, doi:10.1038/s43586-021-00047-w (2021).
- 42 Zhou, X. *et al.* Spinodal Decomposition in Nanocrystalline Alloys. *Acta Mater* **215**, 117054, doi:<https://doi.org/10.1016/j.actamat.2021.117054> (2021).
- 43 Felfer, P., Scherrer, B., Demeulemeester, J., Vandervorst, W. & Cairney, J. M. Mapping interfacial excess in atom probe data. *Ultramicroscopy* **159**, 438–444, doi:<http://dx.doi.org/10.1016/j.ultramic.2015.06.002> (2015).
- 44 Peng, Z. R. *et al.* An Automated Computational Approach for Complete In-Plane Compositional Interface Analysis by Atom Probe Tomography. *Microsc. Microanal.* **25**, 389–400, doi:10.1017/S1431927618016112 (2019).
- 45 da Silva, A. K. *et al.* Phase nucleation through confined spinodal fluctuations at crystal defects evidenced in Fe–Mn alloys. *Nat. Commun.* **9**, 1137, doi:<https://doi.org/10.1038/s41467-018-03591-4> (2018).
- 46 Zhou, X. *et al.* Revealing in-plane grain boundary composition features through machine learning from atom probe tomography data. *Acta Mater* **226**, 117633, doi:<https://doi.org/10.1016/j.actamat.2022.117633> (2022).
- 47 Gault, B. *et al.* Spatial resolution in atom probe tomography. *Microsc. Microanal.* **16**, 99–110, doi:10.1017/S1431927609991267 (2010).
- 48 Gault, B., Moody, M. P., Cairney, J. M. & Ringer, S. P. *Atom Probe Microscopy*. (Springer New York, 2012).
- 49 Jenkins, B. M. *et al.* Reflections on the Analysis of Interfaces and Grain Boundaries by Atom Probe Tomography. *Microsc. Microanal.* **26**, 247–257, doi:10.1017/S1431927620000197 (2020).
- 50 Miller, M., K. The effects on local magnification and trajectory aberrations on atom probe analysis. *J. Phys. Colloques* **48**, C6–565–570, doi:10.1051/jphyscol:1987692 (1987).
- 51 Miller, M. & Hetherington, M. Local magnification effects in the atom probe. *Surf. Sci.* **246**, 442–449, doi:10.1016/0039-6028(91)90449-3 (1991).

- 52 Shibata, N. *et al.* Differential phase-contrast microscopy at atomic resolution. *Nature Physics* **8**, 611-615, doi:10.1038/nphys2337 (2012).
- 53 Müller, K. *et al.* Atomic electric fields revealed by a quantum mechanical approach to electron picodiffraction. *Nat. Commun.* **5**, 5653, doi:10.1038/ncomms6653 (2014).
- 54 Gao, W. P. *et al.* Real-space charge-density imaging with sub-angstrom resolution by four-dimensional electron microscopy. *Nature* **575**, 480-484, doi:10.1038/s41586-019-1649-6 (2019).
- 55 Calderon V, S. *et al.* Atomic Electrostatic Maps of Point Defects in MoS₂. *Nano Letters* **21**, 10157-10164, doi:10.1021/acs.nanolett.1c02334 (2021).
- 56 Fang, S. *et al.* Atomic electrostatic maps of 1D channels in 2D semiconductors using 4D scanning transmission electron microscopy. *Nat. Commun.* **10**, 1127, doi:10.1038/s41467-019-08904-9 (2019).
- 57 Graaf, S. d., Momand, J., Mitterbauer, C., Lazar, S. & Kooi, B. J. Resolving hydrogen atoms at metal-metal hydride interfaces. *Sci Adv* **6**, eaay4312, doi:10.1126/sciadv.aay4312 (2020).
- 58 Hachtel, J. A., Idrobo, J. C. & Chi, M. Sub-Ångstrom electric field measurements on a universal detector in a scanning transmission electron microscope. *Adv. Struct. Chem. Imaging* **4**, 10, doi:10.1186/s40679-018-0059-4 (2018).
- 59 Braithwaite, J. S. & Rez, P. Grain boundary impurities in iron. *Acta Mater* **53**, 2715-2726, doi:<https://doi.org/10.1016/j.actamat.2005.02.033> (2005).
- 60 Krasko, G. L. & Olson, G. B. Effect of boron, carbon, phosphorus and sulphur on intergranular cohesion in iron. *Solid State Communications* **76**, 247-251, doi:[https://doi.org/10.1016/0038-1098\(90\)90832-V](https://doi.org/10.1016/0038-1098(90)90832-V) (1990).
- 61 Tang, S., Freeman, A. J. & Olson, G. B. Local-density studies of the structure and electronic properties of B and S in an Fe grain boundary. *Phys. Rev. B* **50**, 1-4, doi:10.1103/PhysRevB.50.1 (1994).
- 62 Wang, J., Janisch, R., Madsen, G. K. H. & Drautz, R. First-principles study of carbon segregation in bcc iron symmetrical tilt grain boundaries. *Acta Mater* **115**, 259-268, doi:<https://doi.org/10.1016/j.actamat.2016.04.058> (2016).
- 63 Wachowicz, E. & Kiejna, A. Effect of impurities on grain boundary cohesion in bcc iron. *Comput. Mater. Sci.* **43**, 736-743, doi:<https://doi.org/10.1016/j.commatsci.2008.01.063> (2008).
- 64 Cottrell, A. H. Unified theory of effects of segregated interstitials on grain boundary cohesion. *Mater Sci Tech-Lond* **6**, 806-810, doi:10.1179/mst.1990.6.9.806 (1990).
- 65 Hristova, E., Janisch, R., Drautz, R. & Hartmaier, A. Solubility of carbon in α -iron under volumetric strain and close to the Σ 5(310)[001] grain boundary: Comparison of DFT and empirical potential methods. *Comput. Mater. Sci.* **50**, 1088-1096, doi:<https://doi.org/10.1016/j.commatsci.2010.11.006> (2011).
- 66 Larson, D. J. *et al.* Encapsulation method for atom probe tomography analysis of nanoparticles. *Ultramicroscopy* **159**, 420-426, doi:<https://doi.org/10.1016/j.ultramic.2015.02.014> (2015).
- 67 Zhou, X. *et al.* The hidden structure dependence of the chemical life of dislocations. *Sci Adv* **7**, eabf0563, doi:10.1126/sciadv.abf0563 (2021).
- 68 Wachowicz, E. & Kiejna, A. Effect of impurities on structural, cohesive and magnetic properties of grain boundaries in α -Fe. *Modell. Simul. Mater. Sci. Eng.* **19**, 025001, doi:10.1088/0965-0393/19/2/025001 (2011).
- 69 Tschopp, M. A. *et al.* Probing grain boundary sink strength at the nanoscale: Energetics and length scales of vacancy and interstitial absorption by grain boundaries in α -Fe. *Phys. Rev. B* **85**, 064108, doi:10.1103/PhysRevB.85.064108 (2012).
- 70 Kubaschewski, O. *IRON—Binary Phase Diagrams*. (Springer Berlin Heidelberg, 2013).
- 71 Giannuzzi, L. A. & Stevie, F. A. A review of focused ion beam milling techniques for TEM specimen preparation. *Micron* **30**, 197-204, doi:[https://doi.org/10.1016/S0968-4328\(99\)00005-0](https://doi.org/10.1016/S0968-4328(99)00005-0) (1999).
- 72 Giannuzzi, L. A., Drown, J. L., Brown, S. R., Irwin, R. B. & Stevie, F. A. Applications of the FIB lift-out technique for TEM specimen preparation. *Microsc Res Tech.* **41**, 285-290,

- doi:[https://doi.org/10.1002/\(SICI\)1097-0029\(19980515\)41:4<285::AID-JEMT1>3.0.CO;2-Q](https://doi.org/10.1002/(SICI)1097-0029(19980515)41:4<285::AID-JEMT1>3.0.CO;2-Q) (1998).
- 73 Zhou, X., Yu, X.-x., Kaub, T., Martens, R. L. & Thompson, G. B. Grain Boundary Specific Segregation in Nanocrystalline Fe(Cr). *Sci. Rep.* **6**, 34642, doi:10.1038/srep34642 (2016).
- 74 Thompson, K. *et al.* In situ site-specific specimen preparation for atom probe tomography. *Ultramicroscopy* **107**, 131-139, doi:10.1016/j.ultramic.2006.06.008 (2007).
- 75 Jeong, J., Cautaerts, N., Dehm, G. & Liebscher, C. H. Automated Crystal Orientation Mapping by Precession Electron Diffraction-Assisted Four-Dimensional Scanning Transmission Electron Microscopy Using a Scintillator-Based CMOS Detector. *Microsc. Microanal.* **27**, 1102-1112, doi:10.1017/S1431927621012538 (2021).
- 76 Feng, B. *et al.* Atomically ordered solute segregation behaviour in an oxide grain boundary. *Nat. Commun.* **7**, 11079, doi:10.1038/ncomms11079 (2016).
- 77 Gault, B. *et al.* Advances in the reconstruction of atom probe tomography data. *Ultramicroscopy* **111**, 448-457, doi:10.1016/j.ultramic.2010.11.016 (2011).
- 78 Berkels, B. & Liebscher, C. H. Joint non-rigid image registration and reconstruction for quantitative atomic resolution scanning transmission electron microscopy. *Ultramicroscopy* **198**, 49-57, doi:10.1016/j.ultramic.2018.12.016 (2019).
- 79 Zhang, C. Y. *et al.* Optimizing Nonrigid Registration for Scanning Transmission Electron Microscopy Image Series. *Microsc. Microanal.* **27**, 90-98, doi:10.1017/S1431927620024708 (2021).
- 80 Yankovich, A. B. *et al.* Picometre-precision analysis of scanning transmission electron microscopy images of platinum nanocatalysts. *Nat. Commun.* **5**, 4155, doi:10.1038/ncomms5155 (2014).
- 81 Berkels, B. *et al.* Optimized imaging using non-rigid registration. *Ultramicroscopy* **138**, 46-56, doi:<https://doi.org/10.1016/j.ultramic.2013.11.007> (2014).
- 82 Krivanek, O. L. *et al.* Atom-by-atom structural and chemical analysis by annular dark-field electron microscopy. *Nature* **464**, 571-574, doi:10.1038/nature08879 (2010).
- 83 TEMUL Toolkit: <https://temul-toolkit.readthedocs.io/en/latest/index.html>.
- 84 Williams, D. B. & Carter, C. B. *Transmission Electron Microscopy: A Textbook for Materials Science.* (Springer, 2009).
- 85 Ophus, C. Four-Dimensional Scanning Transmission Electron Microscopy (4D-STEM): From Scanning Nanodiffraction to Ptychography and Beyond. *Microsc. Microanal.* **25**, 563-582, doi:10.1017/S1431927619000497 (2019).
- 86 Savitzky, B. H. *et al.* py4DSTEM: A Software Package for Four-Dimensional Scanning Transmission Electron Microscopy Data Analysis. *Microsc. Microanal.*, 1-32, doi:10.1017/S1431927621000477 (2021).
- 87 Dekkers, N. & De Lang, H. Differential phase contrast in a STEM. *Optik* **41**, 452-456 (1974).
- 88 Chapman, J. N., Batson, P. E., Waddell, E. M. & Ferrier, R. P. The direct determination of magnetic domain wall profiles by differential phase contrast electron microscopy. *Ultramicroscopy* **3**, 203-214, doi:[https://doi.org/10.1016/S0304-3991\(78\)80027-8](https://doi.org/10.1016/S0304-3991(78)80027-8) (1978).
- 89 Müller-Caspary, K. *et al.* Measurement of atomic electric fields and charge densities from average momentum transfers using scanning transmission electron microscopy. *Ultramicroscopy* **178**, 62-80, doi:<https://doi.org/10.1016/j.ultramic.2016.05.004> (2017).
- 90 Ehrenfest, P. Bemerkung über die angenäherte Gültigkeit der klassischen Mechanik innerhalb der Quantenmechanik. *Zeitschrift für Physik* **45**, 455-457, doi:10.1007/BF01329203 (1927).
- 91 Pennycook, S. J. & Nellist, P. D. *Scanning Transmission Electron Microscopy: Imaging and Analysis.* (Springer New York, 2011).
- 92 Allen, L. J., D'Alfonso, A. J. & Findlay, S. D. Modelling the inelastic scattering of fast electrons. *Ultramicroscopy* **151**, 11-22, doi:<https://doi.org/10.1016/j.ultramic.2014.10.011> (2015).

- 93 LeBeau, J. M., Findlay, S. D., Allen, L. J. & Stemmer, S. Position averaged convergent beam electron diffraction: Theory and applications. *Ultramicroscopy* **110**, 118-125, doi:<https://doi.org/10.1016/j.ultramic.2009.10.001> (2010).
- 94 Sha, G. & Ringer, S. P. Effect of laser pulsing on the composition measurement of an Al–Mg–Si–Cu alloy using three-dimensional atom probe. *Ultramicroscopy* **109**, 580-584, doi:<https://doi.org/10.1016/j.ultramic.2008.10.012> (2009).

Methods

Bicrystal growth and sample preparation

The presented GB structures were obtained from growing bicrystals of an Fe-Al-B-C alloy with a $\Sigma 5$ GB. An in-house modified Bridgman technique was employed for the sample preparation, in which two seeds were aligned on their common [001] axis and rotated symmetrically with a misorientation of $\Theta = 38^\circ$ perpendicular to their common axis. Further details on the growth of bicrystals are described in our previous publication ⁶. It is worth mentioning that the wet chemical analysis of the bulk sample showed a content of 4 at.% Al, 0.001 at.% B, and 0.05 at.% C. The addition of Al serves to stabilize the bcc-Fe ⁷⁰.

For this work, we cut a disk (5 mm thick and 2 cm in diameter) from the original part of the bicrystal (see Fig. 1). The disk was first polished to obtain a mirror-like surface. Using an FEI Helios Nanolab 600i focused ion beam (FIB) dual beam microscope, we milled a series of marks to determine the location of the GBs. For this sample, a total length of approximately 1 cm GB was found, divided into ROIs from #01 to #91, separated by a horizontal distance of 10 μm between each number (see Extended Data Fig. 1a).

We used transmission electron microscopy (TEM) and APT to analyze the GB structure and composition of four selected ROIs, namely #01, #41, #71, and #91. The in-plane lift-out method (electron beam in TEM perpendicular to the common axis [001] of the grains) was used to prepare the TEM lamellae ⁷¹⁻⁷³. First, the Cu grid was mounted on the correlative holder and placed horizontally in the FIB chamber for the lift-out process. Then, the chamber was vented for rotating the correlative holder 90° to thin the sample. The TEM lamellae were initially thinned to less than 60 nm at an accelerating voltage of 30 kV and then cleanly polished to a thickness of less than 30 nm at an accelerating voltage of 5 kV. The APT tips were fabricated using the conventional FIB lift-out method ⁷⁴. The wedge extracted by the FIB was mounted on a Si coupon and sharpened at 30 kV into needle-like geometries required for field evaporation, with a subsequent 5 kV cleaning step to remove surface damage implanted with Ga^+ .

Orientation mapping

Information on GB character was obtained by EBSD analysis (see Extended Data Fig. 1b) of 9 ROIs (#01-#91) of the polished surface of the bicrystal disk using a JEOL-JSM-6490 microscope operated at 30 kV and equipped with an EDAX/TSL EBSD system. In addition, we performed mapping of the grain orientation and GB characters for the TEM lamellae using precession assistant 4DSTEM ⁷⁵ (see Extended Data Fig. 2). 4DSTEM data sets have been acquired using the TemCam-XF416 pixelated complementary metal-oxide-semiconductor (CMOS) detector (TVIPS) in a JEM-2200FS TEM (JEOL) operated at 200 kV ⁷⁵. During the data acquisition, the incident electron beam was precessed by 0.5° to create a quasi-kinematic

diffraction pattern ^{42,67,73,75} and scanned with a step size of 2.5 nm. The collected diffraction patterns of 4DSTEM data set were indexed by ASTAR INDEX program and the orientation was mapped using an offline TSL OIM Analysis 8 software package.

Atom probe tomography (APT)

In this work, the quantification of GB chemistry was primarily conducted by APT. As for GB chemistry, the composition of a GB can also be measured by energy dispersion spectroscopy (EDS) ⁷⁶ or electron energy loss spectroscopy (EELS) ³⁸. However, the use of these two techniques to study the segregation of B and C at the Fe GBs is not very promising for the following reason: The content of B and C is normally quite low, usually < 2 at. % (see our APT results in Fig. 2).

The GB composition and element distributions of the bicrystals were characterized by APT performed in a Cameca Instruments Local Electrode Atom Probe (LEAP) 5000 XS operated with a specimen set point of 40 K and a laser pulse energy of 30 pJ at a pulse repetition rate of 200 kHz for a 0.5% atoms per pulse detection rate. The collected data sets were reconstructed using the AP Suite 6.1 software platform (See Extended Data Fig. 3). A calibration procedure was applied to obtain the correct image compression factor and k-factor for generating the proper shape and lattice spacing for the reconstructed volume ⁷⁷.

The overall compositions for the reconstructed volume of the tips extracted from ROIs #01, #41, #71, and #91 are $\text{Fe}_{95.47}\text{Al}_{4.34}\text{B}_{0.04}\text{C}_{0.14}$ (at.%), $\text{Fe}_{95.38}\text{Al}_{4.45}\text{B}_{0.07}\text{C}_{0.11}$, $\text{Fe}_{95.37}\text{Al}_{4.38}\text{B}_{0.11}\text{C}_{0.14}$, $\text{Fe}_{95.31}\text{Al}_{4.42}\text{B}_{0.14}\text{C}_{0.14}$, respectively. Here, the peak decomposition algorithm must be applied to quantify the bulk composition because there is significant peak overlapping between Al^+ and Fe^{2+} at 27Da (measured in Daltons, mass-to-charge ratio). The peak decomposition algorithm is only suitable for statistical compositional analyses. It does not provide spatial resolution, e.g., distinguishing compositional differences between two 1 nm³ cubes 1 nm apart. If we want to quantify the one-dimensional (1D) compositional profile across the GB, we need to assign the 27Da to either Al^+ or Fe^{2+} ions. In the 1D composition profile of the Extended Data Fig. 9, the 27Da peak was assigned to the Fe^{2+} ion, resulting in a significantly lower Al content than the value obtained from the wet chemical analysis or the peak decomposition analysis. A more detailed investigation of the Al depletion caused by the co-segregation of B and C can be found in our previous publication ⁶. In the present work, we have mainly focused on the segregation behavior of B and C atoms. It is also worth noting that the local B and C contents obtained from APT composition quantification are significantly higher than the results from the global wet chemical analysis, which is due to GB segregation and a high fraction of GB contained in the reconstructed tip volume.

We used the APT_GB software ⁴⁶ to quantify the in-plane chemical distribution of B and C atoms at the GB, i.e., the composition map and the interfacial excess map (See Extended Data Fig. 3). The GB planes

were identified by a pre-trained convolutional neural network⁴⁶ and meshed triangularly with a unit size of approximately 8 nm². Ladder diagrams were calculated for each vertex of the mesh to determine the interfacial excess and local composition⁴⁶.

The correlation between the local GB compositions of B and C is evaluated using a weighted Pearson product-moment correlation coefficient. A pair of variables (C_B , C_C) represent a pair of B and C compositions of the nodes in the GB meshes. We obtain these composition values from the in-plane chemical distribution described in the previous paragraph. The third variable w corresponds to the area of the nodes. The weighted correlation coefficient is written as

$$\text{corr}(C_B, C_C; w) = \frac{\text{cov}(C_B, C_C; w)}{\sqrt{\text{cov}(C_B, C_B; w)\text{cov}(C_C, C_C; w)}} \quad (1)$$

where weighted covariance $\text{cov}(C_B, C_C, w)$ can be calculated as follow

$$\text{cov}(C_B, C_C; w) = \frac{\sum_i w_i (C_{Bi} - m(C_B; w))(C_{Ci} - m(C_C; w))}{\sum_i w_i} \quad (2)$$

here $m(C_B; w)$ is the weighted mean:

$$m(C_B; w) = \frac{\sum_i w_i C_{Bi}}{\sum_i w_i} \quad (3)$$

High angle annular dark field - Scanning transmission electron microscopy (HAADF-STEM)

All high-resolution HAADF-STEM data were acquired using a Cs probe-corrected FEI Titan Themis 60-300 (Thermo Fisher Scientific) equipped with a high-brightness field emission gun and a gun monochromator operating at 300 kV. Images were recorded with a HAADF detector (Fishe Instruments Model 3000) at a probe current of 68 pA using a semi-convergence angle of 23.6 mrad. The semi-collection angle for high-resolution HAADF-STEM images was set to 103-220 mrad. Image series of at least 20 images were acquired with a dwell time of 2 μ s at a pixel size of 6 pm. To minimize the effects of instrumental instabilities in the images, we used non-rigid registration and averaging of image series to achieve sub-picometer precision measurement of atomic column positions in high-resolution HAADF-STEM images⁷⁸⁻⁸¹. The stacked images were also processed with the Bragg filter and the double Gaussian (band-pass) filter to remove background noise^{82,83}. Extended Data Fig. 5 shows additional high-resolution HAADF-STEM images of ROIs #01, #41, #71, and #91, illustrating the diversity of local GB facet structures. We have also provided the raw stacked images in Extended Data Fig. 10. The boundary planes for these GBs are perpendicular to the paper, resulting in clear imaging conditions for the atomic columns on both sides of the boundary. However, this imaging condition is not always satisfied. Extended Data Fig.

11 shows some HAADF-STEM images of selected ROIs where the top grain overlaps with the bottom grain in the direction perpendicular to the paper.

Atomic four-dimensional STEM (4DSTEM) data collection

The atomic 4DSTEM data were also acquired in the Titan microscope at 300kV. We collected the entire convergent beam electron diffraction (CBED) pattern as a 2D image for each probe position during scanning. These images were taken using an electron microscope pixel array detector (EMPAD) with a readout speed of 0.86 ms per frame (fps) and a linear electron response of 1,000,000:1. Each CBED image has a size of 128×128 pixels. All data sets were acquired with a semi-convergence angle of 23.6 mrad, a defocus value of approximately 0 nm, and a camera length of 300 mm. The exposure time was 1 ms per frame. Beam scanning was synchronized with the EMPAD camera with a scanning step size of 18 pm and a field of view of 2.3×2.3 nm². The scanning step size was optimized by comparing the reconstructed 4DSTEM data sets with step sizes of 13-36 pm. The selection took into account the possibility of minimizing distortions due to instrument instability and maximizing spatial resolution to resolve light atoms. We calibrated the CBED pattern in reciprocal space using the standard Au nanoparticle. Here, each pixel in the CBED pattern is 2.0 mrad.

Electron dose quantification for 4DSTEM data acquisition

Irradiation of materials with accelerated electrons can initiate ballistic knock-on processes that lead to displacement of atoms from the crystal lattice and produce point defects, e.g., a Frenkel pair consisting of an interstitial and a vacancy⁸⁴. For Fe, the maximum transferable kinetic energy at 300 kV is 15.25eV, which is slightly lower than the displacement energy of 16.00 eV⁸⁴. Theoretically, the radiation damage should not be significant when imaging Fe materials. When acquiring atomic 4DSTEM data sets for imaging light atoms at GBs, a lower dose is preferred.

We quantified the dose with the Gatan camera for energy-filtered transmission electron microscopy (EFTEM) by varying the beam via defocusing a monochromator. Extended Data Fig. 12 shows the measured dose as a function of the defocus of the monochromator. The red and blue dots show that the doses for 55 and 95 monochromator defoci are 5.3×10^5 (e⁻/Å²) and 1.9×10^5 (e⁻/Å²), respectively. These two values were used to acquire the atomic 4DSTEM data sets. We did not observe any significant changes in the reconstruction results recorded with these two doses.

Atomic 4DSTEM data reconstruction for experimental data

The originally collected atomic 4DSTEM data contains the 2D grid of the probe position in real space and the 2D diffraction pattern for each probe position in reciprocal space⁸⁵. Data reconstruction is required to

obtain information such as the (virtual annular) dark-field image, the electric field map, the (projected) electrostatic potential map, and charge-density map⁵³ (see Extended Data Fig. 6). The python script pyDPC4D was developed for data reconstruction (GitHub link: <https://github.com/RhettZhou/pyDPC4D>). The script is forked from the py4DSTEM package⁸⁶. We used py4DSTEM to reconstruct the dark-field image and to calculate center of mass (c.m.) of the transmitted beam for each probe position. Our pyDPC4D script mainly focused on the quantitative reconstruction of the electric field map, the (projected) electrostatic potential map, and the charge-density map. The details of the reconstruction are as follows.

Dark field image

The dark-field images are reconstructed from 4DSTEM data sets by integrating the intensity of the annular region of 99-122mrad in the CBED pattern of each probe position. Extended Data Fig. 6a shows an example of the reconstructed dark-field image containing a $\Sigma 5$ (110) // (010) GB.

Electric field map

Atomic electric fields can be measured using DPC-4DSTEM microscopy, an imaging technique that reflects the relative electron probe shifts observed on CBED patterns due to local electric and magnetic fields^{52-54,58,87-89}. This method can resolve the structure of weakly interacting phase objects. For example, when an electron probe passes through an electric field, the electron is deflected due to its negative charge. By quantifying the shifts of the transmitted electron probe in the diffraction plane ($\langle \Delta d^* \rangle$, shift of the c.m.), the change in momentum of the electron probe ($\langle \mathbf{P}_\perp \rangle$) can be calculated. With appropriate modeling, the electric field of the materials under study (\mathbf{E}_\perp) can also be derived. In the simplest model of a uniform electric field, the momentum transfer of the electron is negatively proportional to the electric field. In classical electrodynamics, the electric field is equal to the Lorentz force divided by the charge, which equals the momentum transfer of electrons per time and per charge. According to the Ehrenfest theorem⁹⁰, this also holds in quantum mechanics⁵³. Considering the weak phase object approximation⁹¹ for thin samples, the electron beams move through the sample without changing their velocity in the z direction. The following equation represents the relationship between the momentum transfer ($\langle \mathbf{P}_\perp \rangle$, or shift of the c.m., $\langle \Delta d^* \rangle$) and the measured electric field \mathbf{E}_\perp :

$$\mathbf{E}_\perp = - \langle \mathbf{P}_\perp \rangle \frac{v}{et} = - \langle \Delta d^* \rangle \frac{hv}{et} \quad (4)$$

Here, $v = 2.33 \times 10^8$ m/s is the speed of electrons at 300kV, $e = 1.6022 \times 10^{-19}$ C is the elementary charge, $t \approx 15.0 \times 10^{-9}$ m is the thickness of the specimen, and $h = 6.6261 \times 10^{-34}$ J · s is the Planck's constant.

We applied a circular mask (radius 74 mrad) to the CEBD pattern to calculate the c.m. The purpose of applying mask is twofold. First, it can eliminate intensity from the high-angle scattering that is less sensitive to the momentum transfer than that from the low-angle scattering. Second, it can also reduce the noise from c.m. calculation. Extended Data Fig. 6b shows the c.m. of the electron beam in the vertical (left image) and the horizontal (right image) directions. The electric field can be further calculated according to equation (4) (see Extended Data Fig. 6c for the electric field magnitude).

(Projected) electrostatic potential

We calculated the (projected) electrostatic potential ($\phi(\mathbf{r})$) by integrating the electric field in the plane perpendicular to the electron beam using the following equation.

$$\phi(\mathbf{r}) = - \int_{r_1}^{r_2} \mathbf{E}_{\perp} \cdot d\mathbf{r} \quad (5)$$

Here, \mathbf{E}_{\perp} is the electric field obtained in the previous step. \mathbf{r} is the integrating distance in the real space. We performed the integration by using Fourier transform with the adding of low- and high- pass regularization terms to minimize noise ⁸⁶. Extended Data Fig. 6d presents the reconstruction of the (projected) electrostatic potential of the $\Sigma 5 (110) // (010)$ GB.

Charge-density map

The charge-density can be derived by calculating the divergence of the measured electric field, since they are proportionally correlated according to Gauss's law ^{53,54,89}, see the following equation:

$$\rho = \varepsilon_0 \text{div} \mathbf{E}_{\perp} = -\varepsilon_0 \text{div} \langle \mathbf{P}_{\perp} \rangle \frac{v}{et} = -\frac{\varepsilon_0 h v}{et} \text{div} \langle \Delta d^* \rangle \quad (6)$$

where $\varepsilon_0 = 8.8542 \times 10^{-12} \text{ C}/(\text{V} \cdot \text{m})$ is the permittivity of the vacuum. Assuming that the charge-density is uniform along the z-direction, the (projected) charge-density (number of e^- per area) can be written as:

$$\rho^{N-2D} = -\frac{\varepsilon_0 h v}{e^2} \text{div} \langle \Delta d^* \rangle \quad (7)$$

Extended Data Fig. 6e shows the charge-density map for the $\Sigma 5 (110) // (010)$ GB. We found that light atoms can be well resolved in the reconstructed charge-density map. Therefore, in this work, we will mainly show the charge-density map for imaging light atoms at GBs.

More examples for three representative GB motifs, $\Sigma 5 (110) // (010)$, $\Sigma 5 (310) // (3\bar{1}0)$, and $\Sigma 5 (2\bar{1}0) // (1\bar{2}0)$, are shown in Extended Data Fig. 7, in which light atoms are pointed by black arrows in the charge-density map. For these atomic columns, there is a weak contrast in the ADF image but a relatively strong

contrast in the charge-density map. By comparing GBs with the same misorientation and inclination, different the local motifs can be clearly resolved, for instance, Extended Data Fig. 7a i vs ii for the $\Sigma 5$ (110) // (010) GB, and Extended Data Fig. 7c i-ii vs iii-vi for the $\Sigma 5$ ($2\bar{1}0$) // ($1\bar{2}0$). In addition, defects, such as disconnections and steps, can also strongly affect the local motif and the location of atoms, e.g., Extended Data Fig. 7b iv.

STEM multi-slice image simulation

The purpose for conducting image simulation is twofold. First, we want to estimate the specimen thickness by comparing the experimental and simulated CEBD patterns. Second, the image simulations serve as an important tool to help interpret our experimental results, in particular to validate atomic columns observed by the reconstructed charge-density map. STEM multi-slice simulations were performed using the μ STEM (v5.2) package⁹². We took the $\Sigma 5$ (310) // ($3\bar{1}0$) GB as the model structure for the image simulations. The atomic structure model was based on our DFT study⁶, see Extended Data Fig. 13a, where the red atoms are Fe and the blue atoms are B. The microscope parameters, such as semi-convergence angle (23.6 mrad), primary electron energy (300 kV), and scanning pixel size (18 pm) were identical to the atomic 4DSTEM experimental values. We used the μ STEM package to generate simulated 4DSTEM data sets that have the same format as the experimental data. The rest of the reconstruction was performed using the in-house developed python script pyDPC4D.

Measurement of sample thickness

CBED was acquired to determine the thickness of the TEM sample, because the thickness of the TEM sample has been shown to have a strong effect on the CEBD pattern^{54,93}. Here we have examined some experimental CEBD patterns and compared them with the simulated CEBD patterns. Extended Data Fig. 13b shows three of the experimental CEBD patterns extracted from the 4DSTEM data set with their positions highlighted in purple, orange, and green in the atomic model of the $\Sigma 5$ (310) // ($3\bar{1}0$) GB (see Extended Data Fig. 13a). In the rightmost column of each row, we plotted the position-averaged CBED (PACBED) patterns. Furthermore, we present the reconstructed charge-density maps and the CBED patterns from the same regions for the simulated 4DSTEM data of the $\Sigma 5$ (310) // ($3\bar{1}0$) GB with thicknesses from 4.9 nm to 20.1 nm (see Extended Data Fig. 13c). The thickness of the TEM sample was determined to be 14.9 nm because the experimental (PA)CEBD patterns at such a thickness best match the simulated (PA)CEBD patterns. In addition, we found that the contrast of the atomic columns on the charge-density map became complex patterns instead of a simple circular shape when the sample is thicker than approximately 17 nm. The simulations were performed up to a thickness of 40 nm. An example of the

complex charge-density map can be found in the reconstruction of the 20 nm thick model structure (see the left image in the extended data, Fig. 13c vi).

Atomic 4DSTEM data reconstruction for simulated data

We performed three series of simulations to understand the origin of the contrast appearing in the charge-density map. The benchmark simulation (see Extended Data Fig. 13c v) was performed with a sample thickness of 14.9 nm and a defocus of 0 nm for the atomic structure shown in the Extended Data Fig. 13a.

In the first series, we reconstructed the charge-density maps by systematically changing the defocus from -100 nm to 80 nm (see Extended Data Fig. 8a i-vi). When the defocus is positive, the contrast in the reconstructed charge-density map reversed and appeared as complex patterns (see Extended Data Fig. 8a v-vi). We found it difficult to interpret such reconstruction results. However, the reconstructions produced with negative defocus generally provided good contrast to resolve each of the atomic columns (see Extended Data Fig. 8a i-iii).

The main elements in the bicrystals are Fe, Al, B, and C. In the second series, we investigated the influence of the solute type and structure on the contrast of the charge-density map. The simulated results include interstitial and substitutional B and C sites (see Extended Data Fig. 8b i-iv), Fe sites in the center of the kite structure (see Extended Data Fig. 8b v), and interstitial Al sites (see Extended Data Fig. 8b vi). No difference is apparent in charge density maps reconstructed with B- or C-segregation, regardless of whether they are interstitial or substitutional sites. The DPC-STEM method does not provide mass resolution to distinguish these two light elements. For chemical information, please refer to our APT quantifications. It is worth noting that when the B or C atoms occupy the substitutional sites, a clear contrast can be seen between these atomic columns and the other columns without substitutional sites. We can frequently detect such a contrast difference in the experimental charge-density maps (see Fig. 4 and Extended Data Fig. 7), indicating a possible substitutional occupancy at GBs.

When light B and C atoms occupy the interstitial sites in the center of the kite structure, the contrast in the HAADF image is very weak. The most popular GB motif for the $\Sigma 5$ (310) // (3 $\bar{1}$ 0) GB is the unfilled kite structure, see the HAADF-STEM and dark field images in Fig. 3b, Fig. 4b, Extended Data Fig. 5b, and Extended Data Fig. 7b. The atomic columns of B and C are only visible in the charge-density maps. However, in some cases we can see the contrast in the center of the kite in both the dark field images and the charge-density maps. In these cases, we believe that this contrast comes from the Fe occupation in the kite center, see Extended Data Fig. 8b v. For comparison, we also simulated the charge-density map where Al remains in the kite center as an interstitial site. We can also observe a contrast in the charge-density map, but it appears diffuse, see Extended Data Fig. 8b vi. In the real case, the Al interstitial sites rarely occur for

two main reasons. In our previous work, we found that the Al atoms preferentially occupy the substitution sites instead of the interstitial sites ⁶. Second, there is an Al depletion induced by co-segregation of C and B ⁶. See also the APT results in the Extended Data Fig. 9.

In the last series, we investigated the influence of atom occupancy on the contrast of the charge-density maps (see Extended Data, Fig. 8c). We constructed the GB atomic models containing two B atomic columns: one has 100% atom occupancy, serving as a reference, and the other with a range of atom occupancies between 0% and 100%. It was found that the contrast of the partially occupied atomic column is proportional to the percentage of atom occupancy.

Data availability

The datasets generated or analyzed here are available from the corresponding authors on reasonable request.

Acknowledgements

X.Z. acknowledges the support from Alexander von Humboldt Foundation. X.Z. acknowledge funding by the German Research Foundation (DFG) for funding via project HE 7225/11-1. Work at the Molecular Foundry was supported by the Office of Science, Office of Basic Energy Sciences, of the U.S. Department of Energy under Contract No. DE-AC02-05CH11231.

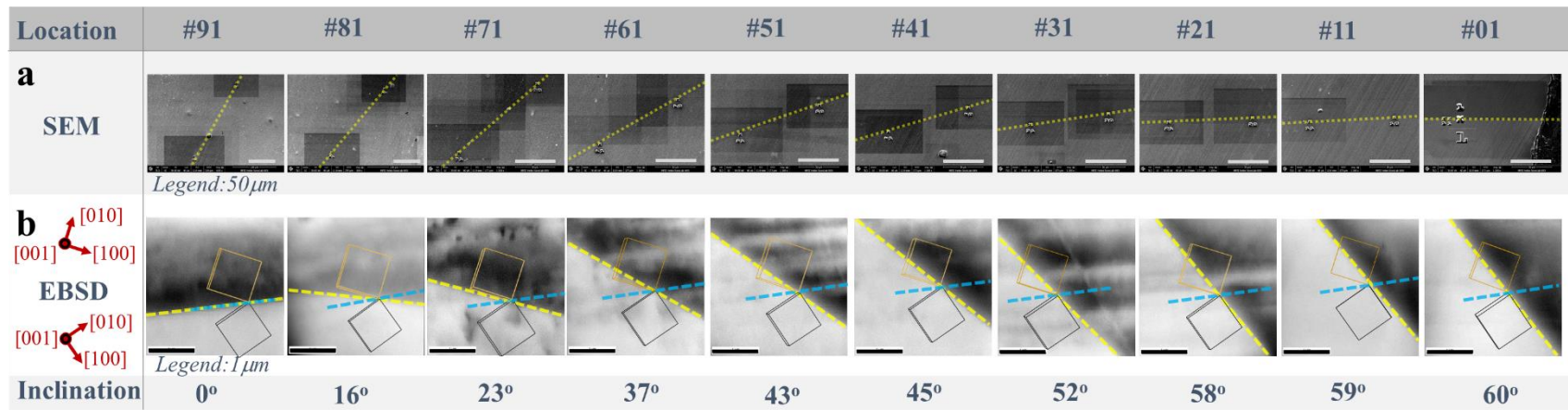
Author contributions

D.R. and G.D. conceived of the presented idea. X.Z. conducted the experiments and analytical characterization. A.A. provided bicrystalline sample. C.H.L. and C.O. guided transmission electron microscopy analysis. B.G. guided atom probe analysis. All authors provided critical feedback and helped shape the research, analysis, and manuscript.

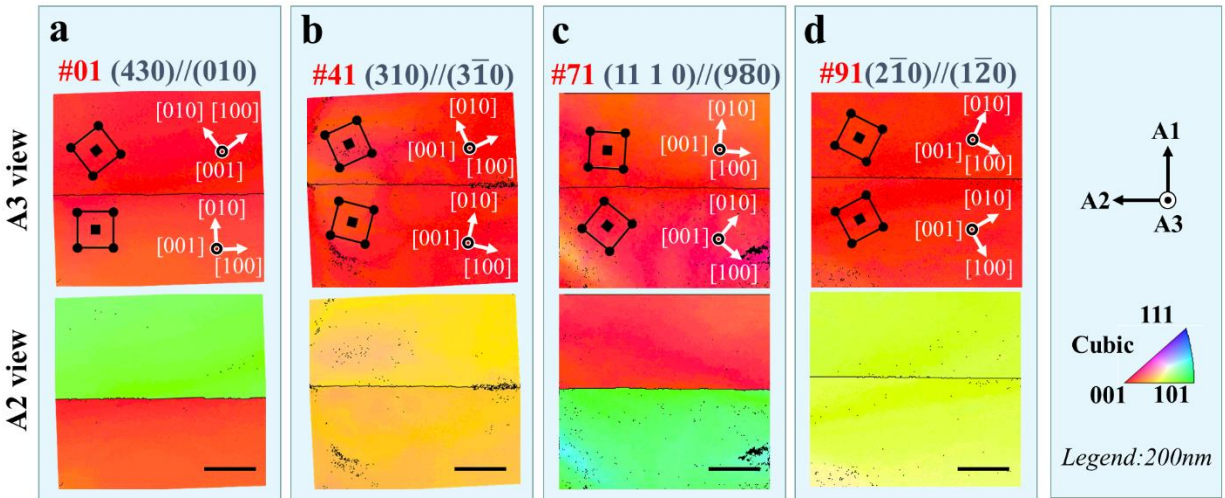
Completing Interests

The authors declare no competing interests.

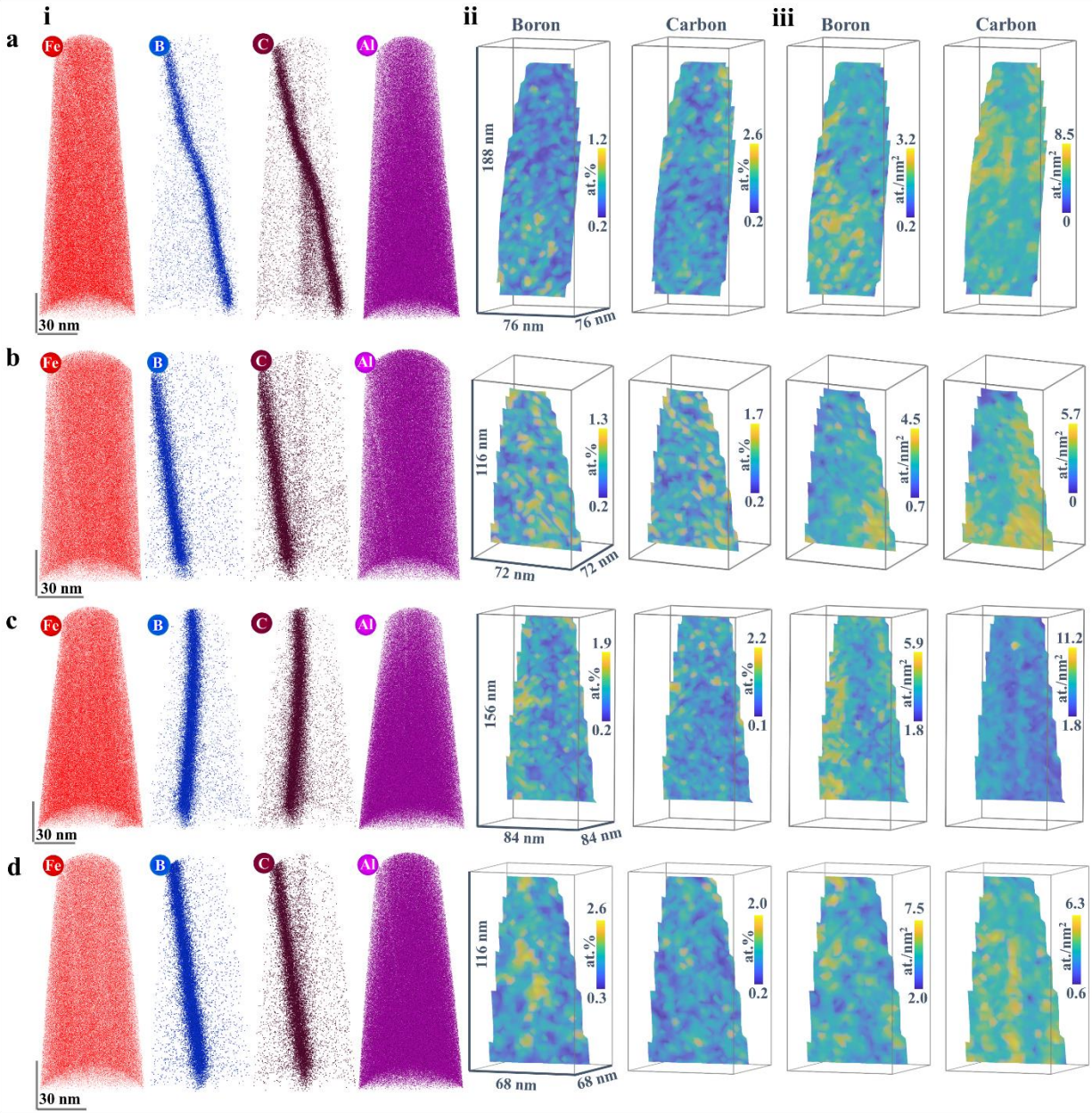
Extended Data Fig. 1 | Scanning electron microscope (SEM) and EBSD characterization of the Fe bicrystal. The [001] tilt $\Sigma 5$ GBs have been obtained by the Bridgman method. The examined GBs have a total length of approximately 1 cm, with the different sections labeled with numbers from #01 to #91. **a** shows the SEM images with the dashed yellow lines superimposed to highlight the GBs. Note that the sample was fixed without rotation during the SEM imaging. The orientation of the GB changed monotonically from one side of the sample to the other. **b** contains the EBSD scans of the sections from #01 to #91. Because the SEM and EBSD images were acquired with different equipment, there is a fixed rotation (approximately 70°) between these two sets of images. In each EBSD sub image, the dashed yellow line indicates the location of the GB. The orange and grey squares mark the orientations of the top and bottom, respectively. The blue dashed line was drawn as the inner angle bisector between the [100] direction of the upper grain and the [010] direction of the lower grain. There are two angle bisectors when considering the translation of the unit cells. Here we consistently use the representation shown in b. With that, the inclination, i.e. the angle between the GB plane and the inner bisector, is listed under each of the EBSD image.



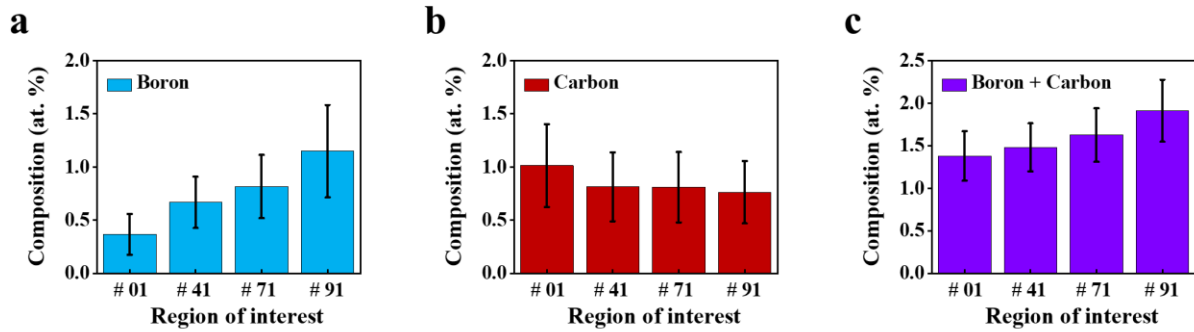
Extended Data Fig. 2 | Nanoscale orientation mapping of $\Sigma 5$ GBs for selected regions. a-d are the reconstructions for GBs #01 (430) // (010), #41 (310) // ($3\bar{1}0$), #71 (11 1 0) // ($9\bar{8}0$), and #91 ($2\bar{1}0$) // ($1\bar{2}0$) from the precession assistant 4DSTEM data sets, to show the A3 view (top images, sample coordinates A1-A3 were defined in the last column of the figure) and the A2 view (bottom images) of the orientation of the grains. The superimposed squares mark the orientations of the grains. The coordination systems for the upper and lower grains are also included in the orientation maps of the A3 view.



Extended Data Fig. 3 | Local chemical composition analysis of $\Sigma 5$ GBs for selected regions. a-d are the APT analyses for GBs #01 (430) // (010), #41 (310) // ($3\bar{1}0$), #71 (11 1 0) // ($9\bar{8}0$), and #91 ($2\bar{1}0$) // ($1\bar{2}0$), respectively. In each row, **i** shows, from left to right, the atom maps of Fe (only show 3 at. % of total Fe atoms), B, C, and Al; **ii** the composition map and **iii** the interfacial excess map of solute B (left) and C (right) for the GBs found in the APT sample shown in **i**.

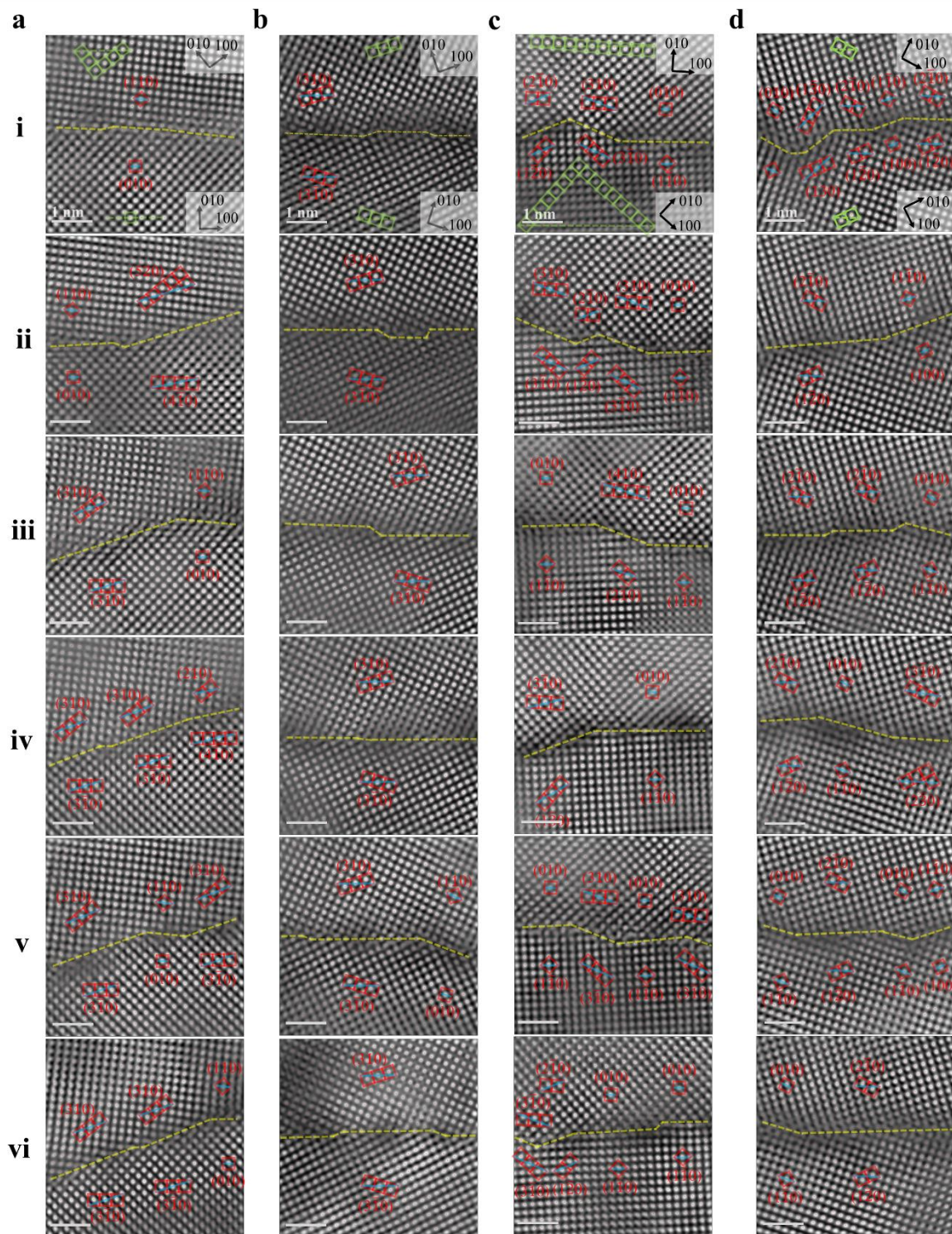


Extended Data Fig. 4 | Summary chart of local chemical compositions of $\Sigma 5$ GBs for selected regions. a-c are the average compositions of boron, carbon, boron and carbon for the GBs of #01 (430) // (010), #41 (310) // (3 $\bar{1}$ 0), #71 (11 1 0) // (9 $\bar{8}$ 0), and #91 (2 $\bar{1}$ 0) // (1 $\bar{2}$ 0), respectively.



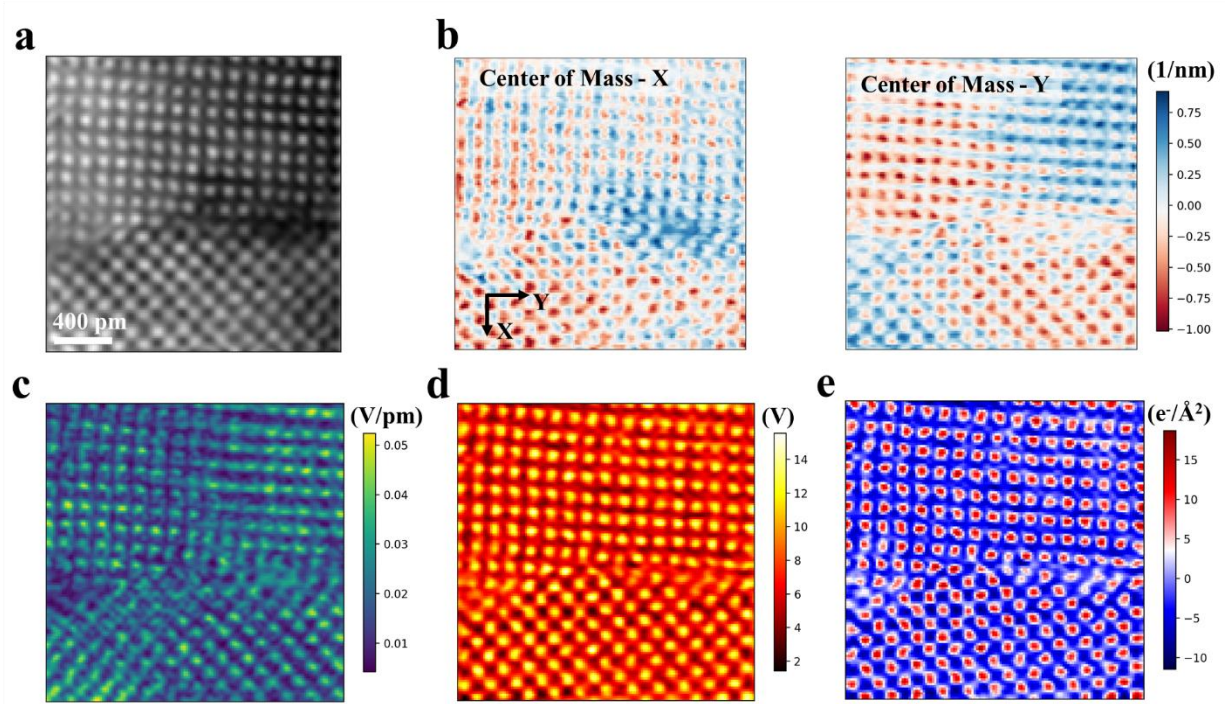
Extended Data Fig. 5 | Analysis of local facet structure of $\Sigma 5$ GBs for selected regions. a-d are high resolution HAADF-STEM images of $\Sigma 5$ GBs with microscopic boundary planes of #01 (430) // (010), #41 (310) // ($3\bar{1}0$), #71 (11 1 0) // ($9\bar{8}0$), and #91 ($2\bar{1}0$) // ($1\bar{2}0$), respectively. The yellow lines indicate

the positions of the GBs. The red squares and blue lines help identify the local GB planes. The green squares and lines help identify the microscopic GB planes.

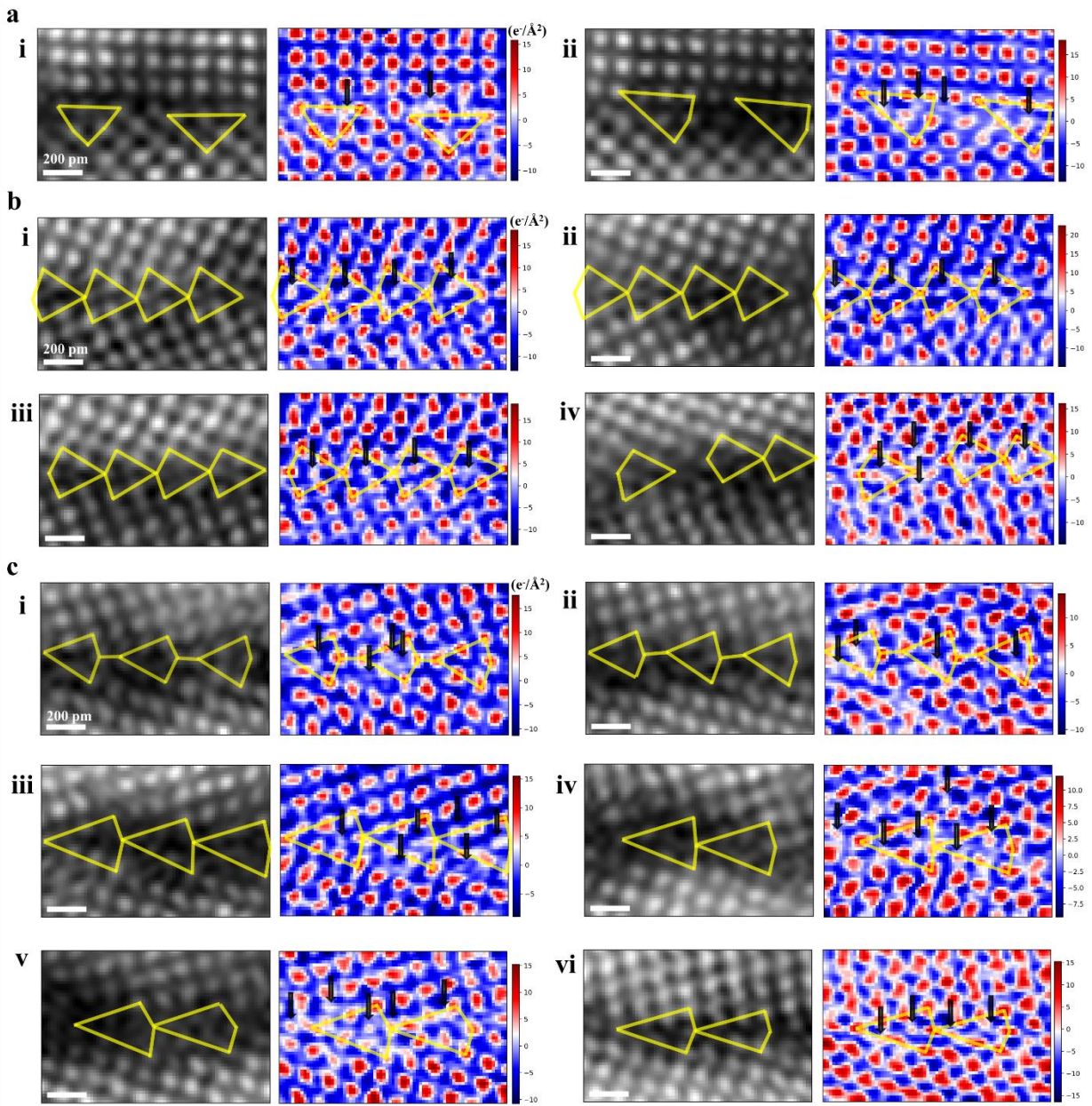


Extended Data Fig. 6 | Experimental DPC-4DSTEM reconstruction for the $\Sigma 5$ (110) // (010) GB. a Reconstructed dark-field image. **b** Change of the center of mass (c.m.) of the transmitted beam in X (left

image) and Y (right image) directions. **c** Electric field magnitude. **d** (Projected) electrostatic potential. **e** Charge-density map.

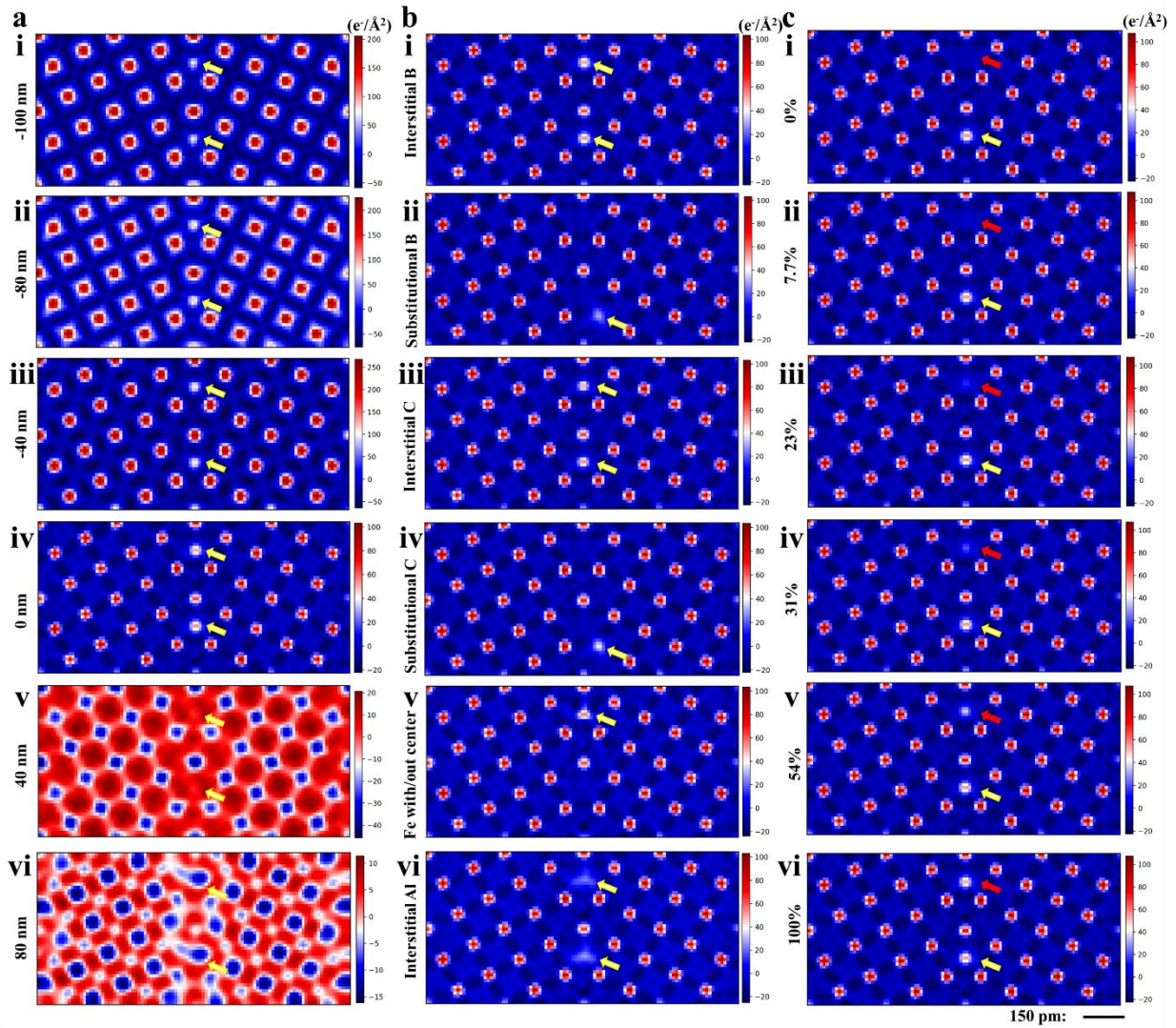


Extended Data Fig. 7 | Light atoms at $\Sigma 5$ GBs for three representative GB motifs: a i-ii $\Sigma 5 (110) // (010)$; b i-iv $\Sigma 5 (310) // (3\bar{1}0)$; c i-vi $\Sigma 5 (2\bar{1}0) // (1\bar{2}0)$. For each GB motif, the left and right image show are the reconstructed dark-field and charge-density map from the atomic DPC-4DSTEM data sets collected in different regions. The repeated structures at GBs have been highlighted in yellow lines. The atomic columns containing B or C are indicated by black arrows in the charge-density maps.



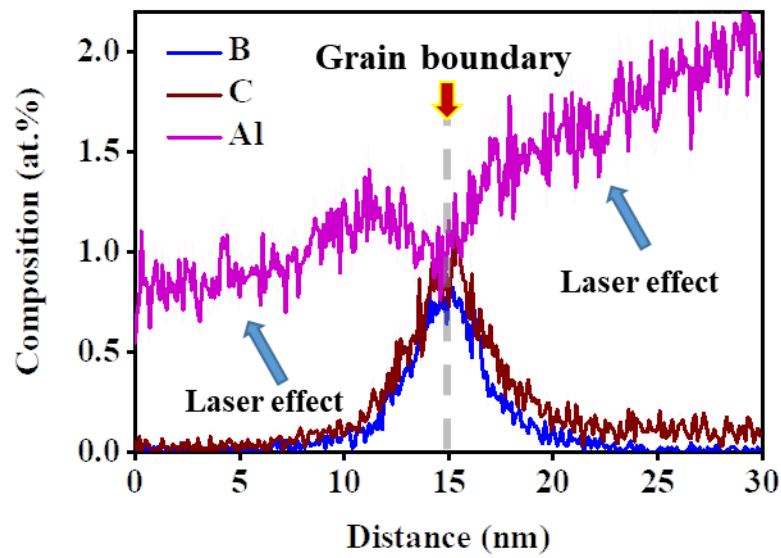
Extended Data Fig. 8 | The influence of defocus, solute type and structure, and site occupancy on the reconstructed charge-density maps from simulated DPC-4DSTEM data sets of the $\Sigma 5$ (310) // $(\bar{3}\bar{1}0)$ atomic GB model. **a i-vi Reconstructed charge-density maps with defocus from -100 nm to 80 nm. **b** Reconstructed charge-density maps for **i** interstitial B sites, **ii** substitutional B sites, **iii** interstitial C sites, **iv** substitutional C sites, **v** Fe sites in the kite center, and **vi** interstitial Al sites. **c i-vi** Reconstructed**

charge-density maps for the occupancy of B sites ranging from 0% to 100%, pointed by the red arrows. The other B atomic columns have 100% atom occupancy, pointed by the yellow arrows, serving as a reference.



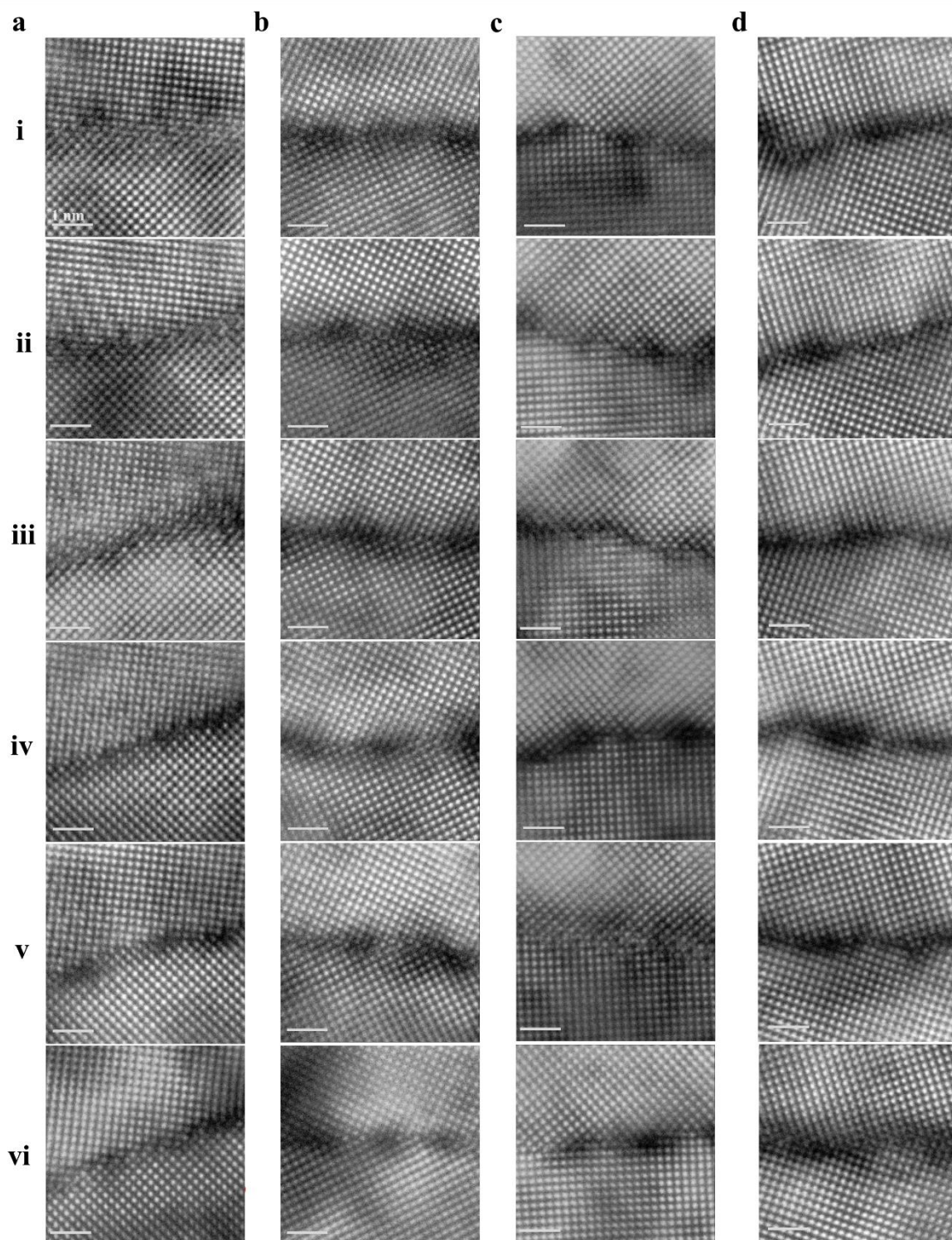
Extended Data Fig. 9 | One-dimensional (1D) line scan across the $\Sigma 5$ (310)//(3 $\bar{1}$ 0) GB. The enrichment of B and C and depletion of Al were observed in the GB region, indicated by the red arrow. The uneven distribution of Al, a gradient of Al content from the left to the right side, is due to the laser artefact⁹⁴. The Al content is lower than its normal chemical composition because the Al⁺ peak overlaps with Fe²⁺. Here we simply assigned the peak at 27Da (measured in Daltons, mass-to-charge ratio) to Fe²⁺.

ions, resulting in a lower measurement of Al content, which is below its nominal value. A more detailed investigation can be found in our earlier publication ⁶.



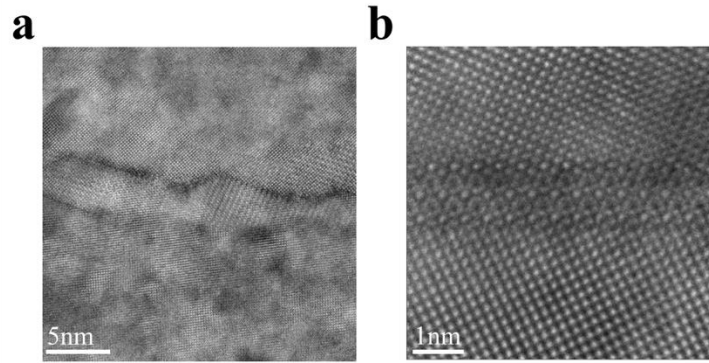
Extended Data Fig. 10 | Analysis of local facet structure of $\Sigma 5$ GBs for selected regions. a-d are raw high resolution HAADF-STEM images of $\Sigma 5$ GBs with microscopic boundary planes of #01 (430) //

(010), #41 (310) // ($3\bar{1}0$), #71 (11 1 0) // ($9\bar{8}0$), and #91 ($2\bar{1}0$) // ($1\bar{2}0$), respectively.

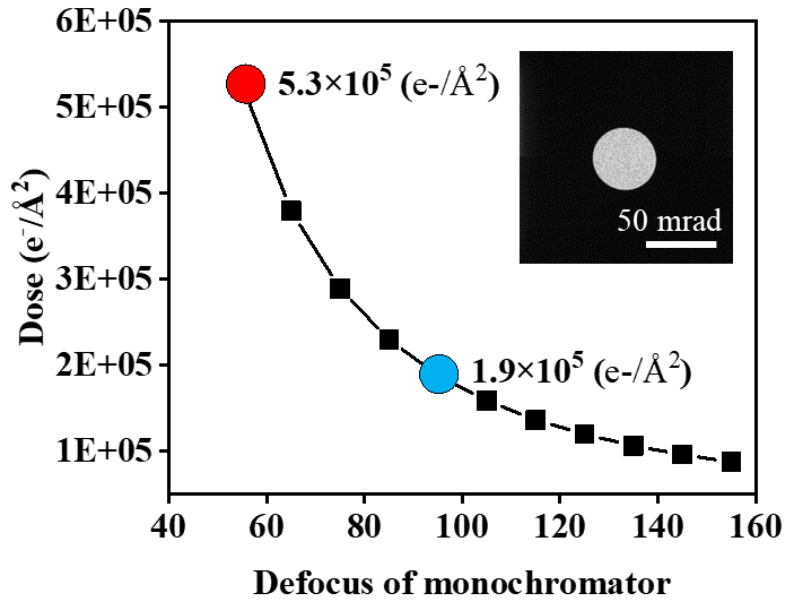


Extended Data Fig. 11 | HAADF-STEM images of selected $\Sigma 5$ GBs to show areas where the top grain overlaps with the bottom grain in the direction perpendicular to the paper. a & b are $\Sigma 5$ GBs

with microscopic boundary planes of #01 (430) // (010) and #41 (310) // ($3\bar{1}0$), respectively. For these types of GBs, the local GB planes cannot be easily determined because they have both tilt and twist characters.



Extended Data Fig. 12 | Electron dose quantification with the Gatan camera for energy-filtered transmission electron microscopy (EFTEM). The red and blue dots show that the dose for 55 nA and 95 nA screen current is 5.3×10^5 ($e^-/\text{\AA}^2$) and 1.9×10^5 ($e^-/\text{\AA}^2$), respectively. These two values were used to acquire the atomic DPC-4DSTEM data sets. The inset gray image shows a reciprocal image of the probe hovering in the vacuum.



Extended Data Fig. 13 | Measurement of sample thickness by convergent beam electron diffraction (CBED). **a** The atomic model structure of the $\Sigma 5$ Fe (colored red) GB with B (blue) decoration. **b** Experimental CBED patterns from the purple, orange, and green highlighted regions, respectively, whose positions are marked with a yellow arrow in a. Position-averaged CBED (PACBED) patterns were also shown in the rightmost column of each row. **c i-vi** Reconstructed charge-density maps (left image) and simulated CBED patterns (right three images) for the $\Sigma 5$ (310) // (3 $\bar{1}$ 0) GB model (see a) with thicknesses from 4.9 nm to 20.1 nm. Simulation results were calculated using μ STEM (v5.2)⁹² and reconstructed using in-house developed Python scripts.

